Simulation of Salt Cavern Abandonment

An Analysis Using SafeInCave

AESM7000: Master Thesis Applied Earth Sciences

Lucas Landeweerd

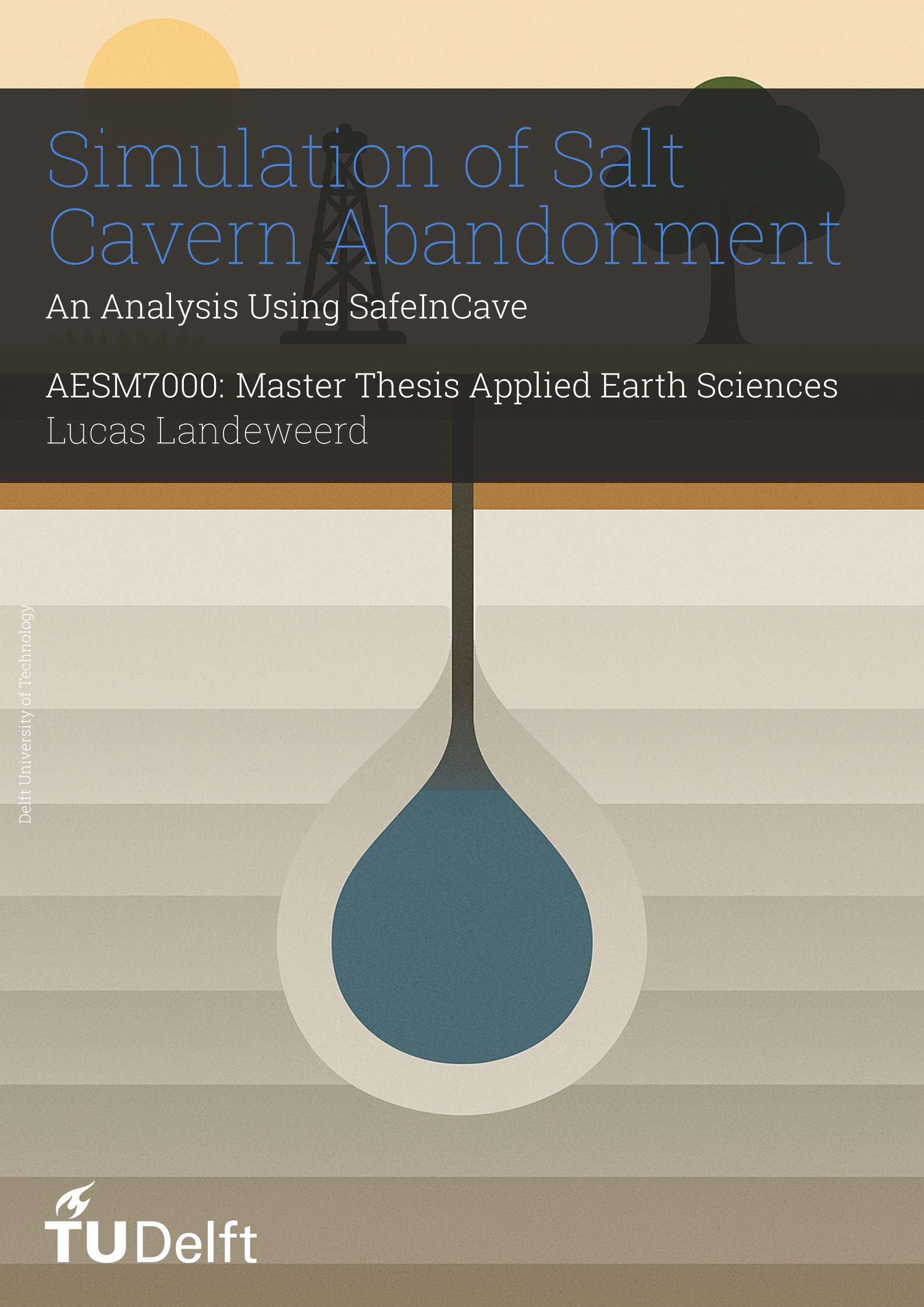

Delft University of Technology

TU Delft

Simulation of Salt Cavern Abandonment

An Analysis Using SafeInCave

by

Lucas Landeweerd

to obtain the degree of Master of Science
at the Delft University of Technology,
to be defended publicly on Friday August 1, 2025 at 10:00 AM.

Student number:	5093554	
Project duration:	October, 2024 – August, 2025	
Thesis committee:	Prof. Dr. H. Hajibeygi,	TU Delft, chair
	Dr. H. T. Honório,	TU Delft, supervisor
	Dr. D. S. Draganov,	TU Delft
	Dr. A. M. H. Pluymakers,	TU Delft

Cover: Self-made, modified using ChatGPT

An electronic version of this thesis is available at http://repository.tudelft.nl/.

TU Delft

Preface

This thesis is submitted in partial fulfillment of the requirements for the Master of Science program in Applied Earth Sciences at Delft University of Technology. The research was carried out between October 2024 and August 2025 and quantifies the mechanical risks that arise when brine-filled salt caverns are abandoned. To this end, the open source finite element simulator *SafeInCave* was extended with a two-way coupling between cavern convergence and the evolving brine pressure.

I am Lucas Landeweerd, a final-year MSc student specializing in Geo-energy Engineering. The work was carried out independently, but in close cooperation with Dr. H. T. Honorio (postdoctoral researcher) and overall supervision from Prof. Dr. H. Hajibeygi.

The report is intended for the thesis committee, for geomechanics researchers, and for practitioners who design, regulate, or operate underground salt-cavern storage facilities. Familiarity with continuum mechanics and basic finite-element concepts is therefore assumed; salt-specific creep mechanisms and abandonment practice are introduced in Chapters 2 and 3.

Readers primarily interested in the constitutive model and simulation workflow may wish to begin with Chapter 3, whereas those seeking a comparison between hard- and soft-shut-in strategies will find the key results in Chapter 4. No prior knowledge of pressure-solution creep is required, as the underlying mechanism and its parameterization are discussed in Section 2.2 before being applied in the subsequent analysis.

I am deeply grateful to Dr. H. T. Honorio for his patient and extensive guidance, and to Prof. Dr. H. Hajibeygi for his incisive feedback and for chairing the committee. I also thank Dr. A. Pluymakers for providing feedback, as well as Dr. D. Draganov for making the time on short notice to take part in the assessment committee. Special thanks go to M. S. Amini for sharing calibration data and to the developer of *SafeInCave* (again Dr. H. T. Honorio) for releasing the code base that underpins this work.

Lucas Landeweerd
Delft, July 2025

Summary

We investigate how creep-driven convergence after cavern abandonment compresses trapped brine and alters geomechanical risk. Using the open-source finite-element simulator SafeInCave, we implement a two-way coupling between cavern volume and hydrostatic brine pressure and run fully coupled simulations for a field-scale cylindrical cavern whose roof lies between 600 m and 2200 m. Two abandonment protocols are considered: *hard shut-in*, in which we permanently seal the well, and *soft shut-in*, in which we vent brine whenever its pressure reaches $70\,\%$ of the overburden stress. Each depth–protocol pair is simulated with and without pressure-solution creep (PSC).

After 300 yr a hard-shut-in cavern loses only $0.30\,\%$ of its initial volume at 600 m and $0.76\,\%$ at 2200 m, yet shallow caverns approach the micro-fracturing threshold as brine pressure climbs to $95\,\%$ of lithostatic pressure. Soft shut-in preserves a ≥ 5 MPa safety margin against microfracturing but allows greater closure: volume loss rises from $1.6\,\%$ at 800 m to $2.4\,\%$ at 1600 m before declining in deeper settings. Convergence initiates faster in deep caverns but decelerates below shallow-cavern rates as deviatoric stresses relax over time. Even in the worst case, 600 m depth under soft shut-in, surface subsidence reaches only 3.1 cm. PSC accelerates early convergence for both protocols; under hard shut-in its influence fades within decades, whereas the constant pressure offset under soft shut-in sustains PSC for centuries, adding ≈ 0.8 cm of subsidence at 800 m but slightly reducing it below 1000 m.

Depth therefore governs post-closure behaviour. Caverns shallower than ≈ 1 km experience rapid pressure build-up that pushes brine pressure to within 1 MPa of lithostatic stress, while deeper caverns become self-limiting and converge slowly. Above 1 km the shut-in protocol dominates risk, whereas below 1 km brine-pressure feedback controls the response. The key findings are:

1. Soft shut-in is essential for caverns with roofs shallower than ≈ 1 km.
2. Hard shut-in suffices at greater depth, as overburden filtering limits surface subsidence to the centimetre range.
3. Future models should incorporate a stress threshold for PSC and stratigraphic layering to avoid over-predicting far-field deformation and rebound.

The coupled-physics workflow developed here thus offers regulators and operators a transparent baseline tool to forecast post-closure deformation, tailor abandonment strategy to depth, and direct monitoring resources where they matter most.

Contents

Nomenclature

Abbreviations

Abbreviation	Definition
DC	Dislocation Creep
FEniCS	Finite–Element Computational Software framework
GMSH	“Gmsh” mesh generator used for cavern meshing
PSC	Pressure Solution Creep

Symbols

Symbol	Definition	Unit
E	Young’s modulus	Pa
g	Gravitational acceleration	$\mathrm{m\,s^{-2}}$
P_{brine}	Brine pressure in cavern	Pa
P_{litho}	Lithostatic pressure at cavern depth	Pa
P_{norm}	Normalised pressure	–
p	Mean stress	Pa
V	Cavern volume	$\mathrm{m^3}$
V_0	Initial cavern volume	$\mathrm{m^3}$
q	Von Mises stress	Pa
s	Deviatoric stress tensor	Pa
Δt	Time-step size	s
u	Displacement vector	m
ϵ	Total strain tensor	–
ϵ_{dc}	Dislocation-creep strain tensor	–
ϵ_e	Elastic strain tensor	–
ϵ_{psc}	Pressure-solution-creep strain tensor	–
κ_T	Isothermal compressibility	$\mathrm{Pa^{-1}}$
ρ	Density	$\mathrm{kg\,m^{-3}}$

1

Introduction

Salt caverns are widely used for underground storage because of their excellent sealing capabilities, mechanical stability, and adaptability to cyclic injection and withdrawal. However, abandonment of such caverns poses significant geomechanical risks, including subsidence, fractures, and brine expulsion into overlying formations. These risks can affect surface infrastructure, groundwater quality, and long-term land stability [18].

Underground hydrogen storage in salt caverns is a promising solution for large-scale energy storage, which is essential to balance the intermittent supply of renewable energy. Salt caverns, in particular, exhibit properties that offer unique advantages, such as low permeability, high mechanical stability, and the ability to withstand cyclic loading. Their performance in storing natural gas and compressed air has already been proven effective, and extending their application to hydrogen storage will significantly aid the transition to a more sustainable energy system [18]. However, despite the benefits of using salt caverns, long-term stability, especially during the abandonment phase, presents significant technical challenges that must be addressed to ensure environmental and structural integrity [18].

The abandonment of salt caverns, once their operational phase ends, can lead to various geomechanical and environmental risks, mainly due to the ongoing creep behavior of salt, subsidence at the surface and the potential expulsion of the contained brine [18]. When a cavern is abandoned, it undergoes gradual deformation driven by the convergence of rock salt (creep), which can lead to significant subsidence over time. Different abandonment strategies such as hard shut-in (fully plugged cavern), soft shut-in (controlled maximum pressure) and open flow (unplugged cavern) impact the behavior of cavern closure and surface deformation in different ways [9]. Investigating these scenarios is necessary to determine the safest and most effective long-term abandonment approach.

The geomechanical response of the cavern in the abandonment phase is influenced by factors such as its brine pressure, salt-creep behavior, cavern depth, and the presence of impurities within the salt structure itself [24]. That is, four processes occur that influence the pressure of the brine: cavern convergence, brine heating, brine leakage through the well, and brine percolation through the walls of the cavern. We focus on **the effect of cavern convergence only**, providing a baseline for the addition of the other processes in the future. As the cavern converges, a reduction in its volume occurs, leading to compression of the brine contained within. This compression results in an increase in brine pressure, attributed to the lack of pressure management during the abandonment phase. The elevated brine pressure exerts force upon the cavern walls, consequently decelerating the convergence process. This feedback mechanism is crucial to understanding the evolution of brine pressure in abandonment scenarios, especially under hard shut-in conditions. Although existing research has explored cavern stability during the operational phase, limited studies have focused on post-abandonment behavior and pressure evolution.

To address these knowledge gaps, we will adapt and use the SafeInCave simulator, a finite-element modeling tool designed to analyze the mechanics of salt caverns [11]. Simulating different abandonment strategies enables a systematic assessment of long-term risks such as subsidence patterns,

stress redistribution, and structural failure potential. The results will provide insight into the optimization of abandonment procedures to enhance safety and environmental sustainability. These insights contribute to optimizing abandonment protocols, promoting safer practices, and informing regulatory frameworks. With the ongoing expansion of hydrogen storage, the implementation of responsible closure strategies for salt caverns is crucial to ensuring public trust and minimizing environmental impacts.

1.1. Research Questions

As salt caverns transition to their post-operational phase, it becomes essential to evaluate the mechanical and environmental risks that may arise. Although previous studies address the aspects of cavern behavior during operation, there remains a limited understanding of how abandonment strategies influence long-term subsidence, fracturing, and brine expulsion. We aim to fill this gap by simulating and analyzing key geomechanical processes during abandonment using the SafeInCave simulator, and answer the following questions under the explicit assumption of brine compression being the sole driver of pressure change:

1. **What are the risks associated with cavern abandonment?**
   (a) How does subsidence develop over time?
   (b) When do fractures form and brine percolation occur in abandoned caverns?
   (c) How does cavern depth influence these risks?
2. **How do different abandonment options impact these risks?**
   (a) What is the effect of a hard shut-in on subsidence and brine percolation?
   (b) How does a soft shut-in influence long-term cavern convergence and fracturing potential?
   (c) How does cavern depth alter the risks under various abandonment strategies?
3. **How does the inclusion of pressure solution creep affect these aspects?**
   (a) How does depth influence the effect of pressure solution creep?

2

Background

This chapter puts together key information that underpins the remainder of the thesis. First, Section 2.1 describes how salt bodies form, how caverns are leached, and how they are operated for gas and hydrogen storage. Next, Section 2.2 seperates the elastic, viscoelastic, viscoplastic, dislocation-creep and pressure-solution-creep responses that control cavern convergence over time. Section 2.3 contrasts hard shut-in, soft shut-in and open-cavern scenarios, tracing the feedback between pressure build-up and long-term convergence. The subsequent Section 2.4 compiles the mechanical and environmental hazards of subsidence, fracturing and brine expulsion that emerge once active pressure regulation ceases. Section 2.5 then explores how geometry, burial depth and host-rock heterogeneity affect these processes. Finally, Section 2.6 sets out the simulation framework and hypotheses tested in this work, providing a roadmap for the chapters that follow.

2.1. Salt Caverns

Salt caverns used for energy storage are typically artificially created cavities within underground salt formations, formed through controlled leaching of halite beds or domes. Their low permeability, high mechanical integrity, and deformation characteristics make them ideal for storing pressurized gases such as natural gas, compressed air, and hydrogen.

2.1.1. Geological Setting

Salt deposits originate from the evaporation of ancient seas, forming thick layers of halite and other evaporites such as anhydrite and gypsum [23]. These can occur as bedded salt formations, with horizontal halite layers often interbedded with claystone, shale, or carbonate rock, and are relatively heterogeneous [8]. In such a formation, the salt content refers to the percentage of the halite layers compared to the total. Salt deposits also occur as domal salt structures, formed by the upward buoyant movement of salt through the overburden (a process known as diapirism) [16]. This process results in a more homogeneous, vertically extensive salt body, which is preferred for cavern development. The larger thickness of domal deposits allows for taller caverns with larger volumes than those in bedded formations, which tend to be shorter and wider.

2.1.2. Cavern Creation

Salt caverns are formed via solution mining, where freshwater is injected into a well to dissolve the salt. The resulting brine is extracted and used in industry or otherwise discharged into the ocean [24]. The geometry of the cavern, which is shaped during leaching, is of great importance to the geomechanical stability of the cavern both during operation and during abandonment. In a simple configuration, two annular tubes are placed in a salt formation, one deeper than the other. The shape can be controlled by injecting water into the top (to favor expansion of the upper part) or at the bottom (to favor expansion of the lower part) [18]. This is also known as indirect and direct leaching, respectively [24]. The use of a blanket pad (normally diesel or nitrogen) protects the roof of the cavern from excessive leaching and allows more control over the dimensions of the cavern [24]. Caverns formed by direct leaching tend to

be cylindrical in shape, while caverns formed by indirect leaching have an enlarged upper section [24]. More complex well configurations allow for different cavern shapes, such as horizontal caverns, which can be more feasible in thinner bedded salt structures [24].

2.1.3. Operation

Once leaching is complete and the desired shape of the cavern is achieved, cushion gas is injected to replace the brine. This gas, usually nitrogen, provides the cavern with the minimum pressure needed to maintain stability. [24]. Therefore, deeper caverns tend to be more expensive to operate due to the larger amount of cushion gas required. After leak testing is conducted, the cavern enters operation, where it is cyclically injected with hydrogen, which is subsequently extracted on demand. The maximum operating pressure is limited by the lithostatic pressure of the salt formation, as approaching this value would result in cracking of the formation that forms percolation pathways [24]. The minimum and maximum operating pressures are usually set in the range of 24% and 80% of overburden pressure, respectively, to ensure safety [24].

2.2. Geomechanical Behavior of Salt

Salt caverns exhibit different mechanical behaviors due to the unique properties of halite and the long-term stress-dependent deformation mechanisms that govern salt rock. These properties contribute to their sealing capacity, but also present challenges during abandonment due to their time-dependent convergence.

Halite, the primary component of rock salt, is nearly impermeable, allowing for the long-term retention of stored gas or brine. It also shows ductile behavior under geostatic loading, which gives rise to self-healing of fractures and creep-driven deformation. The low permeability and high solubility in water make halite a good seal but also susceptible to dissolution via groundwater flow.

Rock salt experiences time-dependent deformation known as creep, a result of impure defects in its lattice structure [29]. This deformation occurs in three stages: primary, secondary, and tertiary [31]. The primary stage consists of transient creep where dislocation movement occurs quickly leading to more strain, while tertiary creep is characterized by the spread of microcracks and eventual brittle failure [18]. In the scope of cavern abandonment, secondary creep is the most relevant, which encompasses both dislocation-creep and pressure solution creep (PSC) [18]. dislocation-creep, the most well-studied of the two, dominates at higher deviatoric stresses between 5-20 MPa [15]. These different deformation mechanisms can be decomposed into elements of springs and dashpots forming a series that represents a constitutive model of the mechanics of salt.

The constitutive model used in this study is similar to the ones presented in [13] [12], which is also implemented in the SafeInCave simulator. In these papers, a constitutive model was formulated for rock salt that undergoes cyclic loading, splitting the total strain into a sum of four smaller strain tensors [13]. This has been modified by adding PSC to the total strain:

$$\varepsilon = \varepsilon_e + \varepsilon_{ve} + \varepsilon_{vp} + \varepsilon_{dc} + \varepsilon_{psc} \tag{2.1}$$

where ε_e represents the instantaneous elastic response, ε_{ve} represents the viscoelastic response, ε_{vp} the viscoplastic response, ε_{dc} the dislocation-creep strain and ε_{psc} the PSC strain. Notably, in the model proposed by Herminio et al. (2024), PSC was not taken into account as the deviatoric stresses were greater than 5 MPa and could be neglected [13]. This is not always the case with cavern abandonment, as the deviatoric stresses decrease over time as the lithostatic pressure approaches.

2.2.1. Elastic Strain

The elastic strain element of the salt-rock constitutive model, ε_e, is represented by defining a fourth-order elasticity tensor $\mathbf{C}$ that depends on Poisson's ratio ν: $\mathbf{C} = \mathbf{C}(\nu)$, mapping real values to a $3 \times 3 \times 3 \times 3$ matrix

$$\mathbf{C} : \mathbb{R} \longrightarrow \mathbb{R}^{3\times3\times3\times3},$$

with components

$$C_{ijkl}(\nu) = \frac{\nu}{(1+\nu)(1-2\nu)}\,\delta_{ij}\,\delta_{kl} + \frac{1}{2(1+\nu)}\big(\delta_{ik}\,\delta_{jl} + \delta_{il}\,\delta_{jk}\big), \tag{2.2}$$

where δ_{ij} is the Kronecker delta [13].

Assuming the material is an isotropic linearly elastic solid, the elastic strain tensor at time t_i follows from

$$\varepsilon_e(t_i) = \mathbf{C}_1^{-1} : \sigma(t_i), \tag{2.3}$$

where the constitutive fourth-order tensor $\mathbf{C}_1$ is defined as

$$\mathbf{C}_1 = E_1\,\mathbf{C}(\nu_1). \tag{2.4}$$

E_1 and ν_1 are Young's modulus and Poisson's ratio that characterize the elastic response of the material, found via calibration to be equal to 102 GPa and 0.32, respectively [13].

2.2.2. Dislocation-Creep Strain

Dislocation-creep is a time-dependent deformation mechanism in crystalline materials, driven by the movement of dislocations through the crystal lattice under differential stress. In salt, dislocation-creep becomes the dominant process under moderate to high deviatoric stresses >5 MPa [18]. At the microscopic level, dislocation-creep involves the thermally activated glide and climb of dislocations past obstacles within the crystal lattice [20]. This process becomes more active at higher temperatures and stresses, but is grain-size insensitive [19], leading to a nonlinear relationship modeled using an Arrhenius-type power-law equation [13]:

$$\dot{\varepsilon}_{dc} = A_{dc}\exp\left(-\frac{Q_{dc}}{RT}\right) q^{n_{dc}-1}\boldsymbol{s}, \tag{2.5}$$

where dc denotes dislocation-creep, Q_{dc} is the activation energy in J/mol, q is the von Mises stress, $\boldsymbol{s}$ is the deviatoric stress, R is the universal gas constant, T is temperature in Kelvin, and A_{dc} and n_{dc} are material parameters, found by Herminio et al. (2024) via calibration to be 3.0 and 1.1×10^{-21} Pa^{n}s^{-1} respectively [13]. Using equation 2.5, ε_{cr} at time t_i can be computed using

$$\varepsilon_{dc}(t_i) = \varepsilon_{dc}(t_{i-1}) + \Delta t\dot{\varepsilon}_{dc}(t_i), \tag{2.6}$$

where $\Delta t = t_i - t_{i-1}$.

In the SafeInCave simulator, dislocation-creep is treated as a viscoplastic process without a yield surface such that any nonzero deviatoric stress leads to creep deformation [11].

Importance of dislocation-creep

Although differential stresses around a cavern decrease after shut-in, they rarely vanish completely. Soon after the leaching stops and the cavern is filled with brine (hard shut-in) or maintained at a controlled pressure (soft shut-in), stress magnitudes can remain well above the < 5 MPa range which PSC dominates [15]. Dislocation-creep governs the deformation of salt around caverns wherever the differential stress > 5 MPa [15]. Neglecting dislocation-creep can therefore contribute to the under-prediction of convergence rates, especially at the beginning of cavern closure.

2.2.3. Pressure Solution Creep

Pressure solution creep (PSC) is a thermally activated time-dependent deformation mechanism that occurs in granular rocks such as halite under conditions of low deviatoric stress (>5 MPa) found in the far field or during abandonment [15]. It is the dominant deformation mechanism in the low-stress domain, with experimental data showing a linear stress dependence [27].

PSC involves the dissolution of stressed grain boundaries, diffusion of dissolved material through the brine, and subsequent precipitation at less stressed sites, favored by smaller grain sizes [26]. This process slows down once the stress is below a yield stress value, which is when grain boundary healing negates the effects of PSC [28]. This yield stress is theorized to be in the range of 0.07 - 0.7 MPa [15].

To capture the first-order affects of PSC in long-term abandonment simulations, we use the same general power-law Arrhenius formulation as for dislocation-creep (equation (2.5)), but with a linear stress dependence ($n = 1$).

$$\dot{\varepsilon}_{psc} = A_{psc} \exp\left(-\frac{Q_{psc}}{RT}\right) q^{1-1} \boldsymbol{s} = A_{psc} \exp\left(-\frac{Q_{psc}}{RT}\right) \boldsymbol{s}, \tag{2.7}$$

where psc denotes the parameters for PSC. An equation similar to equation (2.6) can be used to compute the total strain:

$$\varepsilon_{psc}(t_i) = \varepsilon_{psc}(t_{i-1}) + \Delta t \dot{\varepsilon}_{psc}(t_i), \tag{2.8}$$

Importance of Pressure Solution Creep

In the constitutive model examined by Herminio et al. (2024), PSC was omitted, as the majority of experimental studies referenced in the literature used stress levels exceeding 5 MPa, which was also the stress range relevant to their investigation [13]. Since that paper was written, further experimental data has been collected, allowing calibration of the parameters in equation (2.7) [1]. Ignoring PSC in numerical models leads to underestimation of strain rates in low-stress regions and time periods, which is especially true for caverns at shallow depths (e.g., 1100-1600 m depth) or late in abandonment [15].

2.2.4. Viscoplastic Strain

Primary creep, which consists of transient creep, is the initial stage of time-dependent deformation during which the strain rate progressively decreases under constant load, reflecting the microstructural accommodation of stress before reaching steady-state creep conditions [19]. The transient creep is represented by ε_{vp} in the constitutive model presented by Honorio et al. (2024)[13]. It can be captured with a Perzyna-type overstress model [17]:

$$\dot{\varepsilon}_{vp} = \mu_1 \left\langle \frac{F_{vp}}{F_0} \right\rangle^{N_1} \frac{\partial Q_{vp}}{\partial \sigma} \tag{2.9}$$

where $\langle \cdot \rangle$ is the Macaulay ramp, μ_1 and N_1 are material parameters, and F_0 is a reference value. The associative (i.e., $Q_{\mathrm{vp}} = F_{\mathrm{vp}}$) yield function [13] reads:

$$F_{\mathrm{vp}}(\alpha, \boldsymbol{\sigma}) = J_2 - \left[-\alpha I_1^{n_1} + \gamma I_1^2\right] \left[e^{\beta_1 I_1} + \beta \frac{\sqrt{27}\, J_3}{2\sqrt{J_2^3}}\right]^m, \tag{2.10}$$

with invariants

$$I_1 = \operatorname{tr} \boldsymbol{\sigma} + \sigma_t, \qquad J_2 = \tfrac{1}{2}\mathbf{s} : \mathbf{s}, \qquad J_3 = \det \boldsymbol{\sigma},$$

s the deviatoric stress tensor and n_1, γ, β_1, β and m being material parameters. The size of the yield surface evolves through:

$$\alpha = \frac{a_1}{\left[(a_1/\alpha_0)^{1/\eta} + \xi\right]^{\eta}}, \qquad \xi = \int_{t_0}^{t} \sqrt{\dot{\boldsymbol{\varepsilon}}_{\mathrm{vp}} : \dot{\boldsymbol{\varepsilon}}_{\mathrm{vp}}}\, \mathrm{d}t, \tag{2.11}$$

where a_1, α_0 and η are material parameters and ξ is the accumulated viscoplastic strain [13]. Using the viscoplastic strain rate $\dot{\boldsymbol{\varepsilon}}_{\mathrm{vp}}(t_i)$, the total viscoplastic strain $\boldsymbol{\varepsilon}_{\mathrm{vp}}(t_i)$ can be computed implictly:

$$\varepsilon_{vp}(t_i) = \varepsilon_{vp}(t_{i-1}) + \Delta t \dot{\varepsilon}_{vp}(t_i), \tag{2.12}$$

Viscoplasticity in abandonment

During abandonment, the brine pressure increases steadily toward lithostatic pressure. This increase in mean stress reduces the deviatoric component J_2 that drives the yield function in equation (2.10). When $F_{\text{vp}} < 0$, the Macaulay operation in equation (2.9) vanishes and the formulation then predicts $\dot{\varepsilon}_{\text{vp}} = 0$. According to Brouard et al., "creep rate is a highly non-linear function of applied deviatoric stress" [7], meaning that raising brine pressure slows cavern convergence. In the abandonment phase, characteristic pressure build-up spans months to years, so the stress path moves into the elastic domain and remains there. Therefore, viscoplastic strain can be neglected for abandonment simulations.

2.2.5. Viscoelastic Strain

Reverse transient creep is a recoverable and time-dependent strain that occurs during the unloading and reloading cycles, manifesting as hysteresis in the stress-strain response [13]. The Kelvin-Voigt spring-dashpot captures the time-dependent elastic (viscoelastic) response of the rock, and when a stress σ is applied to this element, it is balanced by the spring and dashpot in parallel:

$$\sigma = \underbrace{\mathbf{C}_2 : \varepsilon_{ve}}_{\text{spring}} + \underbrace{\eta_2 \dot{\varepsilon}_{ve}}_{\text{dashpot}}, \tag{2.13}$$

in which $\mathbf{C}_2$ is the fourth-order stiffness tensor, η_2 is the viscosity of the dashpot, and ϵ_{ve} is the spring and dashpot's deformation [12]. This equation can be solved for $\dot{\epsilon}_{ve}$, leading to equation 2.14

$$\dot{\varepsilon}_{ve} = \frac{1}{\eta_2} \left(\boldsymbol{\sigma} - \mathbf{C}_2 : \varepsilon_{ve} \right), \tag{2.14}$$

The time-dependent compliance tensor of the Kelvin-Voigt element is

$$\mathbf{C}_2^{-1}(t) = \frac{1}{E_2} \left(1 - \mathrm{e}^{-\frac{E_2}{\eta_2} t} \right) \mathbf{C}^{-1}(\nu_2), \tag{2.15}$$

E_2 and ν_2 are the Young's modulus and Poisson's ratio of the spring, respectively, and η_2 is the viscosity of the dashpot.

Viscoelasticity in abandonment

During abandonment, the cavern is isolated, and its brine pressure only changes slowly through brine/thermal equilibriation. This can be orders of magnitude lower than the pressure ramps applied during normal operation. Looking at equation 2.15, it can be seen that the time taken for the strain to decrease to $1 - \frac{1}{e} \approx 0.632$ is equal to $\tau = \eta_2 / E_2$ where τ is the characteristic retardation time [3]. In the calibration study for these parameters by Herminio et al. (2024), $\eta_2 \approx 2.5 \times 10^{14}$ Pa s and $E_2 \approx 4.2 \times 10^{10}$ Pa [13], so $\tau \approx 6000$s ≈ 1.7h. Argyris et al. show that the recoverable strain becomes "nearly zero" once the time step $\Delta t >> \tau$ [2]. Cavern abandonment involves pressure changes spread over months to years, several orders of magnitude longer than τ, hence any Kelvin-Voigt element would fully relax long before the next time step. Therefore, the viscoelastic element will not be used in the constitutive model for this study.

2.3. Abandonment Strategies and Their Effects

The post-operational phase of a salt cavern is heavily influenced by the chosen abandonment strategy. These strategies determined how brine pressure evolves over time, thus governing the stress distribution and creep behavior of the cavern during closure. When a cavern is sealed, the brine pressure is equal to the wellhead pressure, which is considered to be the initial pressure for the abandonment phase [9]. This section presents the main abandonment scenarios studied in the literature and evaluates their implications.

2.3.1. Hard Shut-in

The hard shut-in strategy involves completely sealing the cavern at the end of its operational life without any mechanism for controlled pressure relief. As the salt creeps inward and the cavern volume decreases, the brine pressure increases due to compression, which results in the brine exerting more force on the cavern walls. Eventually, the cavern pressure approaches the lithostatic pressure of the overburden. This reduces deviatoric stresses and slows creep. Therefore, hard shut-in is generally associated with less long-term subsidence compared to other abandonment methods. However, it can also initiate brine infiltration if microcracks open in the cavern wall if the cavern pressure gets close enough to the lithostatic pressure [9].

2.3.2. Soft Shut-in

In soft shut-in, the cavern pressure is managed by intermittently releasing brine to keep the pressure below a critical threshold. For example, pressure may be reduced by 10 bar once it reaches a preset limit [9]. A pressure equal to 70% of geostatic stress is a conservative limit for soft shut-in [15]. By regulating the maximum brine pressure, microfracturing can be better controlled, limiting the chances of brine infiltration.

Since the cavern pressure remains below lithostatic pressure levels, the deviatoric stress is higher than in hard shut-in, resulting in faster creep and higher levels of cavern convergence. This leads to more surface subsidence above the cavern. Therefore, soft shut-in requires long-term supervision and is considered a compromise between structural safety and surface deformation.

2.3.3. Open Cavern (No Shut-in)

In this scenario, the cavern is left open to the surface, resulting in a brine pressure equal to the pressure of the wellhead. This low brine pressure results in high deviatoric stresses and rapid cavern closure due to accelerated creep.

Although brine pressure build-up is avoided, open abandonment strategies are seldom used due to their tendency to promote uncontrolled deformation and operational unpredictability.

2.3.4. Summary

The three abandonment strategies can be compared, summarized in Table 2.1:

Table 2.1: Comparison of Salt Cavern Abandonment Strategies.

Strategy	Pressure Evolution	Creep Behavior	Implications
Hard Shut-in	Pressure increases due to brine compression; approaches lithostatic pressure levels	Slowed creep due to reduced deviatoric stress	Minimal long-term subsidence; risk of brine infiltration via microcracks [9]
Soft Shut-in	Pressure managed via intermittent brine release; remains below lithostatic pressure	Moderate creep due to higher deviatoric stress	Requires long-term monitoring; balances structural integrity and subsidence control [9]
Open Cavern (No Shut-in)	Pressure remains low (at wellhead pressure)	Fast creep due to high deviatoric stress	Promotes rapid cavern closure; rarely used due to instability and deformation risk

2.4. Risks During and After Abandonment

The abandonment of salt caverns marks the end of active management and the beginning of a long-term geomechanical evolution driven by time-dependent deformation processes in salt. Although salt caverns are generally safe during operation due to tight control of brine pressure, their stability becomes uncertain once pressure regulation stops. This section explains the various mechanical and environmental risks that emerge during the post-operational phase of cavern life including subsidence,

fractures, and brine percolation.

2.4.1. Subsidence and Convergence

As salt continues to deform via creep, the shape of the cavern changes and the volume decreases with time through convergence. This reduction in subsurface volume is transmitted upward through the overburden, producing surface deformation. Subsidence typically forms a shallow bowl-shaped depression, but the magnitude and rate depend on the cavern geometry, surrounding geology, and the abandonment scenario [9].

A hard shut-in scenario, where the cavern is sealed and no pressure is relieved, leads to a gradual pressure increase inside the cavern due to brine compression. As the brine pressure approaches the lithostatic pressure, convergence continues in the lower cavern zones and subsidence progresses [9]. Although subsidence in this scenario is generally smaller than in other strategies, it can still be significant on long timescales [9].

In contrast, a soft shut-in scenario, in which the brine is intermittently released to limit the brine pressure to a chosen threshold, leads to more rapid convergence and increased subsidence. The lowest resistance to creep and the highest subsidence occurs in the open (no shut-in) case, where the cavern pressure remains low and the stress differentials are high. Modeling efforts have predicted measurable surface deformation for up to 200 years after abandonment, depending on the conditions [9].

Including a linear, PSC branch in the constitutive model increases the subsidence predicted for an abandoned cavern. In finite-element runs where linear ($n \approx 1$) PSC was added to the dislocation formulation (power law), Hunfeld et al. (2022) showed that both the cavern convergence and the transmitted surface bowl deepen by almost an order of magnitude compared to the creep of power law alone [15]. Their parametric study also found that a threshold is necessary to prevent overestimation of subsidence [15].

The subsidence rebound of several centimeters in magnitude is a process observed in several subsidence modeling studies [6] [22] [4]. If rock salt creep becomes linear (as with PSC at low stresses), it can lead to such an effect [22]. However, it was also found that there is no rebound when salt creeps through power law alone [22]. This rebound effect is pronounced when linear creep is modeled with no threshold value, allowing far-field salt flow to progress [4]. This process has not yet been observed in abandoned hydrocarbon reservoirs, but the authors propose that it may be due to the long period of time required to observe rebound [22].

2.4.2. Fracturing and Brine Percolation

As the cavern closes and pressure increases, microcracks can open in the cavern wall, particularly near the roof, where the salt is weaker [9]. When the difference between brine pressure and lithostatic pressure is <1 MPa, brine percolation begins [9]. This process, called pressure-driven percolation, creates secondary permeability in the otherwise tight salt, allowing the brine to infiltrate the surrounding rock mass. As the pressure of the brine increases, the infiltration of the brine begins shortly before the lithostatic pressure is reached [9]. This process starts at the cavern roof, where the lithostatic pressure is the lowest. As abandonment progresses, convergence continues to take place in the lower part of the cavern, further driving brine infiltration in the upper part of the cavern [9].

Over time, infiltration can extend beyond the salt formation and into the overburden, particularly in bedded salt formations. This is especially concerning because interbedded layers may have higher permeability, which facilitates brine migration. These processes represent a key risk to both the integrity of the cavern and the quality of the groundwater.

2.4.3. Accelerated Creep and Long-Term Uncertainty

In the post-abandonment phase, the deviatoric stresses decrease over time as the brine pressure increases. This shifts the dominant deformation mechanism from dislocation-creep (which is generally accepted to dominate at deviatoric stresses >5 MPa to pressure solution creep, which operates at lower stress (see Figure 2.1) and is also grain-size sensitive [18]. Long-term tests found that in the range of 0.2 - 5 MPa, pressure solution creep was the main creep mechanism [9]. However, PSC may cease below a certain threshold, which means that the deformation may stall or slow down depending on local

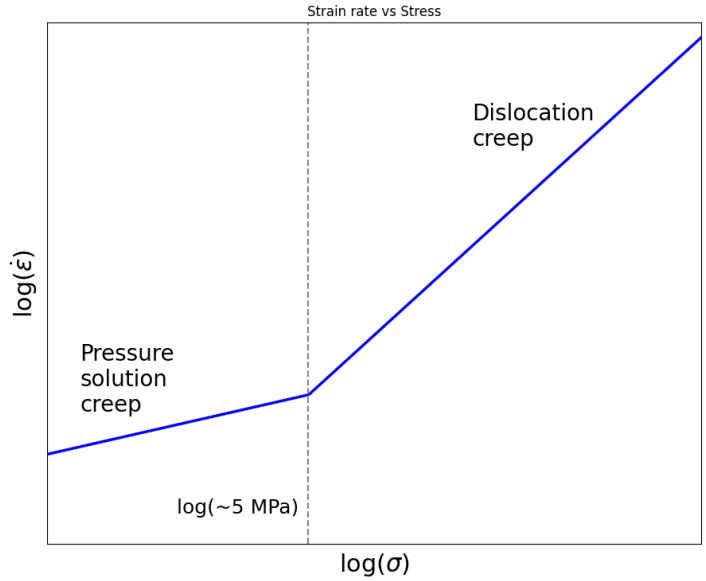

Figure 2.1: Transition from dislocation-creep dominated strain to a pressure solution creep dominated strain, adapted from Kumar et al. [18]

stress states [15].

Many simulations neglect pressure solution creep due to its slow nature and lack of relevance during operational phases due to relevant deviatoric stresses. However, it is highly relevant when investigating cavern abandonment and neglecting pressure solution creep risks underestimating long-term convergence and subsidence by up to a magnitude [15].

In extreme cases, the continuous creep and stress redistribution may lead to a localized loss of stability or roof failure, potentially triggering a partial or full cavern collapse. This risk is particularly pronounced in bedded salt with weak interlayers or irregular geometries, where tertiary creep and microcracking can evolve into macroscopic failure if not mitigated through proper abandonment strategies [24].

2.5. Cavern Shape, Depth, and Material Influence

Industrial storage caverns are commonly leached as upright cylinders that can maximize possible storage volume, particularly in domal deposits [24]. Indirect leaching can create an enlarged head that changes its stress profile. Irregular-shaped caverns can lead to concentrations of high stress that lead to local failure zones [19]. For horizontal caverns in bedded salt formations, a deeper and narrower subsidence trough occurs under the same loading conditions [30]. The cross-sectional diameter and length have realistic maximums, due to the nonlinear increase in both construction time and long-term surface deformation [30].

The lithostatic pressure increases with depth, and increasing the depth of the cavern increases the rate of steady-state creep displacement [19]. The higher mean stress also delays the transition to the PSC-dominated displacement, because the deviatoric stress remains above 5 MPa for longer periods [15]. In a study by Hunfeld et al., a standard cavern was defined as being located at a depth of approximately 1100 m, while a deep cavern was located at a depth of approximately 2100 m [15]. Deeper caverns tend to be more unattractive for storage due to the requirement for more cushion gas due to higher lithostatic pressure [24].

Domal salt is almost pure halite and mechanically homogeneous, while bedded salt contains anhydrite, dolomite, or shale layers that introduce stiffness and permeability contrasts and potential percolation pathways [24]. During leaching, these less soluble layers can create irregular shapes that can act as stress concentration points leading to early failure [24]. Different salts can also exhibit different creep parameters, in some cases ranging from $n = 3$-6 [7].

2.6. Research Focus

This thesis investigates how the abandonment of brine-filled salt caverns triggers mechanical and environmental risks through time-dependent deformation processes. By simulating cavern closure across a range of depths and abandonment scenarios, the goal is to explore how creep-driven convergence, brine pressure evolution, and surface subsidence are shaped by key abandonment decisions.

To that end, the SafeInCave simulator is extended to incorporate volume-pressure feedback. This allows a direct comparison between hard and soft shut-in while capturing the influence of cavern depth on deformation modes. A PSC model is included as well, so its effect can also be investigated.

A central point of our work is that the dominant creep mechanism varies systematically with the depth and pressure of the cavern. Dislocation-creep, with its higher activation energy Q_{dc}, becomes increasingly dominant at depth due to elevated temperatures. In contrast, in shallow caverns or late in abandonment when deviatoric stresses falls below 5 MPa, PSC is expected to govern the deformation. This transition may be more pronounced under soft shut-in, where pressure is regulated 30% below lithostatic pressure, allowing persistent differential stress.

Another key hypothesis relates to the impact of subsidence on the surface. Although deeper caverns are subjected to higher geostatic loads and may exhibit higher levels of convergence, they also experience stronger feedback from pressure build-up, potentially limiting long-term subsidence. Shallower caverns, especially those under soft shut-in, may show prolonged convergence, and hence higher cumulative subsidence. The comparative evaluation of these responses will help clarify the trade-offs between abandonment effort (active pressure management) and long-term risk reduction (subsidence, brine percolation).

By systematically varying depth, abandonment strategy, and creep mechanisms, we aim to generate a comparative data set that provides further information on how these parameters interact. The results are expected to support the development of targeted mitigation strategies aligned with site-specific geological and operational constraints.

3

Methodology

The purpose of our study is to simulate the geomechanical behavior of salt caverns during the abandonment phase, with a focus on subsidence, stress redistribution, and the interaction between cavern pressure and rock-convergence evolution. This is done using the SafeInCave simulator, a finite-element tool designed to simulate the time-dependent deformation of salt caverns [14].

For this thesis, the simulator is extended to include a coupling between brine pressure and cavern convergence. As the cavern deforms, the internal volume changes, which affects the pressure of the brine inside. This updated pressure is then used as a boundary condition on the cavern wall in the next time step, forming a feedback loop. A new module is used to calculate the volume of the deformed cavern mesh at each time step and then calculate the brine pressure based on a compressibility law. These modifications allow the SafeInCave simulator to better capture the evolving mechanical state of a cavern during abandonment, where pressure is not actively controlled.

We perform a range of simulations that test different abandonment strategies (hard, soft and open), cavern depths, and the effect of enabling or disabling pressure solution creep on long-term evolution.

3.1. Simulator Description: SafeInCave

All simulations in this thesis are performed using SafeInCave, an open-source finite-element simulator developed to study the mechanical response of salt formations under various storage and loading conditions. The simulator is written in Python and built on top of the FEniCS framework, using tetrahedral meshes and non-linear mechanics to solve for displacement fields and stress evolutions [11].

SafeInCave follows a modular structure in which the behavior of salt is described through a configurable constitutive model. Each simulation solves the quasi-static momentum balance for small deformations, with the total deformation partitioned into elastic, viscoelastic, viscoplastic and creep contributions [11]. These are assembled from mechanical analogues such as linear springs (giving an instantaneous elastic response), Kelvin-Voigt dashpots (viscoelasticity), and time-dependent components such as creep and viscoplasticity.

All simulation setups are configured via a single JSON input file, which specifies the mesh path, time schedule, solver parameters, boundary conditions, body forces, and constitutive law. A GMSH grid must be provided that represents the cavern's geometry and the surrounding layers. The user can define time-dependent Neumann and Dirichlet conditions with spatial variation, such as depth-dependent overburden or pressure gradients along the cavern wall.

For numerical integration, fully implicit, Crank-Nicolson, and explicit schemes are supported by SafeInCave [11]. For this study, the Crank-Nicolson scheme will be used. A consistent tangent matrix is used to linearize the governing equations, allowing for a robust Newton-based solution even under highly nonlinear creep regimes. This ensures that the code remains stable during long-term simulations, where strains accumulate gradually.

The simulator allows for two phases: equilibrium and operation. The equilibrium stage applies initial geostatic stresses and creep effects under a constant cavern pressure until a steady state is reached. Only then does the operation stage begin, during which pressure conditions can be varied. This allows for clean initialization of stress fields and avoids numerical instability in early time steps.

Post-processing is enabled through a Paraview compatible output in *Visualization Toolkit* (VTK) file format, as well as Python-based tools for extracting displacements, strains, and volumes over time. Internally, PyTorch is used for tensor operations, and all material models operate on a per-element basis, allowing spatial heterogeneity if desired.

3.2. Constitutive Model Selection

The constitutive model used in this thesis includes elastic deformation and dislocation creep for all simulations, with optionally enabled PSC depending on the scenario. The relevant total strain equation for abandonment is

$$\varepsilon = \varepsilon_e + \varepsilon_{dc} + \varepsilon_{psc} \tag{3.1}$$

The rationale for this selection is discussed in Section 2.2. Elasticity is included to capture the instantaneous response of both the salt and the surrounding overburden. Dislocation-creep is the dominant mechanism under moderate to high deviatoric stresses, which remain relevant even during abandonment, particularly in the early stages or near the cavern wall. In contrast, PSC becomes important at lower differential stresses and is particularly active during long-term abandonment or in shallow caverns. Since PSC was not originally implemented in SafeInCave, it is added during the course of this thesis using parameters calibrated by a PhD researcher working in parallel [1].

Elastic Parameters

Linear elasticity is applied to all regions of the mesh. For the salt domain, a Young modulus of $E_{\text{salt}} = 102$ GPa is used, found through the calibration by Honorio et al. (2024) [13]. For the overburden, a value of $E_{\text{overburden}} = 15$ GPa is selected to represent a generic overburden. A Poisson ratio of $\nu = 0.32$ iss used uniformly for both materials, also calibrated for salt by Honorio et al. (2024) [13]. These values fall within the published ranges for a generic overburden [25], reflecting the mechanical properties relevant for long-term simulations.

Dislocation Creep

Dislocation creep is included as the baseline inelastic deformation mechanism. The following parameters are used: $A_{dc} = 1.1 \times 10^{-21}\text{Pa}^{-3}, \text{s}^{-1}$, a stress exponent of $n = 3.0$, and an activation energy of $Q_{dc} = 51{,}600\text{J mol}^{-1}$ [13]. This corresponds to a stress-sensitive, temperature-activated mechanism that is active across most of the cavern wall under differential stress. It is included in all simulation runs, including those where PSC is also enabled.

Pressure Solution Creep

PSC is implemented using a spatially varying pre-exponential term A_{psc} that depends on depth [1]. This dependency reflects the temperature gradient with depth, as PSC is known to be thermally activated. Using equation (2.7), and setting $n = 1$, $Q_{psc} = 13,184$ J/mol, the spatial dependence of A_{psc} is calculated as:

$$A_{psc}(z) = \frac{B_{psc}}{T(z)}, \tag{3.2}$$

where $B_{psc} = 1.29 \times 10^{-13}\text{KPa}^{-1}, \text{s}^{-1}$and $T(z)$ is the temperature profile [1].

This function is passed to the simulator as a spatial field and its intensity increases with depth due to the temperature profile [1]. The temperature gradient used is 27 K/km, and the surface temperature was fixed at 20°C.

Together, this model setup allows for direct comparison between dislocation-dominated and PSC-dominated convergence regimes, particularly under different cavern depths and abandonment strategies.

3.3. Coupled Brine-Pressure Feedback

Coupling cavern convergence to brine compression is crucial to accurately simulating the abandonment of salt caverns. As the cavern deforms due to creep, it converges and its volume shrinks. This in turn causes a pressure response from the brine as it compresses due to the cavern shrinkage. This increase in pressure alleviates deviatoric stress in the salt, slowing creep. Representing the interplay between mechanical deformation and fluid behavior is essential in order to use SafeInCave to simulate long-term cavern abandonment. Only volume loss from salt creep influences brine pressure; brine temperature, and mass exchange through the well and cavern walls is not included, consistent with the scope defined in the introduction.

3.3.1. Isothermal Compressibility

The isothermal compressibility of a fluid describes the differential change in volume due to a change in pressure at a constant temperature:

$$\kappa_T \equiv -\frac{1}{V}\left(\frac{\partial V}{\partial p}\right)_T, \tag{3.3}$$

where κ_T is the isothermal compressibility, V is the volume, and p is the pressure. The negative sign reflects that an increase in pressure typically causes a decrease in volume. Treating the derivatives as differentials and rearranging:

$$-\kappa_T dp = \frac{dV}{V}. \tag{3.4}$$

Integrating pressure and volume and assuming κ_T to be constant throughout the interval, we get

$$-\kappa_T \int_{p_1}^{p_0} dp = \int_{V_0}^{V_1} \frac{dV}{V}. \tag{3.5}$$

Evaluating the integrals results in the following:

$$\ln(V_1) - \ln(V_0) = -\kappa_T(P - P_0). \tag{3.6}$$

Rearranging gives a direct relation between pressure and volume change:

$$P_1 - P_0 = \frac{1}{\kappa_T} \ln\left(\frac{V_0}{V_1}\right). \tag{3.7}$$

Equation (3.7) is used to update the brine pressure inside the cavern at each time step based on the computed volume change. As SafeInCave did not employ existing volume computations, we also implement this first (see Appendix A for code). The isothermal compressibility, κ_T, is obtained from CoolProp's thermophysical-property database, using the values for pure water as there was none for brine. CoolProp is an open-source library that provides high-accuracy thermodynamic properties for pure fluids and mixtures [5]. Because it allows κ_T to be set as an explicit function of both temperature and pressure, this choice keeps the compressibility fully consistent with the simulated cavern conditions. For all simulations, the isothermal compressibility is evaluated at a fixed reference temperature of 300 K. This is necessary because CoolProp returns $\kappa_T(P, T)$, but cavern-scale temperature variations are not tracked in the present formulation.

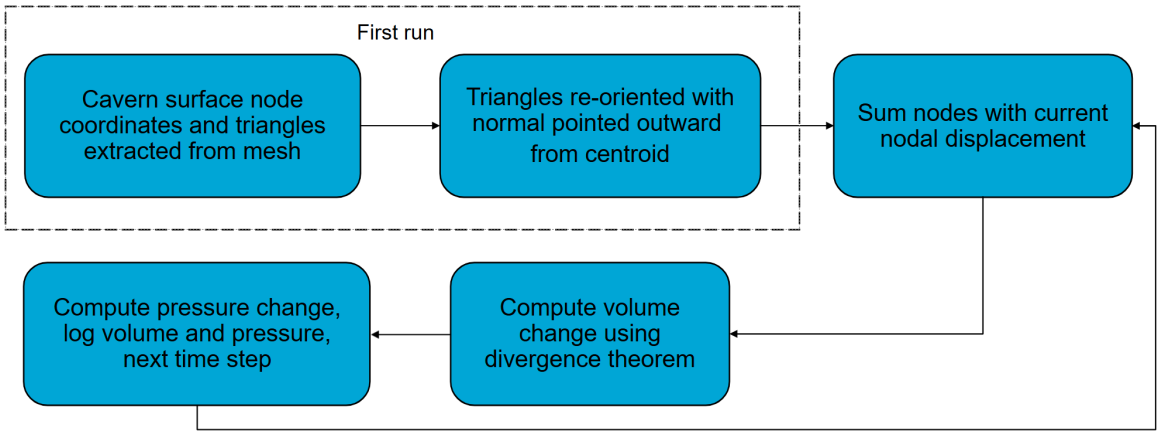

Figure 3.1: Workflow for Volume Computation in SafeInCave.

3.3.2. Volume Computation

To compute the volume of the cavern at each time step, the cavern surface mesh is first extracted from the input GMSH grid. This includes the coordinates of the mesh nodes and the list of triangular facets that make up the cavern wall. SafeInCave uses unstructured tetrahedral meshes, and the outer boundary of the cavern is identified by its boundary tag in the input file. A centroid-based method is used to consistently orient all surface triangles outward.

The volume of the cavern is then computed using divergence theorem. For a closed surface discretized into triangles, the enclosed volume V can be calculated from the mesh as:

$$V = \sum_i \frac{1}{6} \left(\vec{v}_i \cdot (\vec{v}_j \times \vec{v}_k) \right), \tag{3.8}$$

where $\vec{v}i, \vec{v}j, \vec{v}_k$ are the coordinates of the three vertices of triangle i. This is equivalent to summing the signed volumes of tetrahedra formed by each surface triangle and the origin. Because the triangle orientation is outward facing, the computed volume is positive.

At each time step, the displacement field $\mathbf{u}$ is applied to the original mesh coordinates to obtain the deformed surface. The current volume $V(t)$ is then calculated using the updated nodal coordinates. This volume is passed to the brine compression equation (3.7) and stored for post-processing. This process is handled automatically by the `VolumeMonitor` class inside the SafeInCave framework. Figure 3.1 shows the workflow for volume computation.

Now that the volume can be computed, the resultant pressure can be imposed as a boundary condition.

3.3.3. Coupling

Once the mean brine pressure is calculated using the compressibility law, it is converted into a hydrostatic pressure profile and applied along the cavern wall. This is done by evaluating the pressure at each point z on the cavern boundary using the formula:

$$P(z) = P_{\text{mean}} - \rho g (z_{\text{bottom}} - z), \tag{3.9}$$

where ρ is the density of the brine, g is the gravitational acceleration, and z_{bottom} is the depth of the cavern bottom. This ensures that pressure varies with depth, mimicking the hydrostatic behavior of brine.

This pressure profile is applied as a special Neumann boundary condition in the simulator. During the equilibrium stage, this condition is initialized on the basis of the input pressure and cavern geometry. In the operation stage, it is updated at every Newton iteration using the newly computed volume and displacement field until the error tolerance is reached.

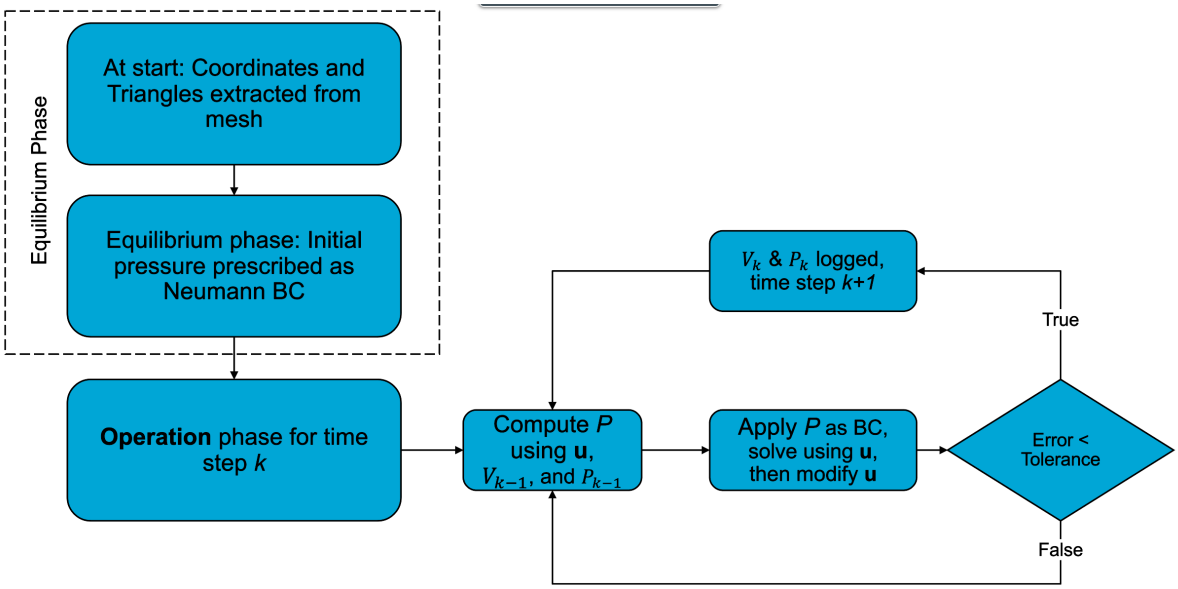

Figure 3.2: Flowchart showing how pressure is coupled to cavern convergence.

By applying this hydrostatic gradient directly to the surface mesh, SafeInCave captures the self-regulating nature of the brine pressure during cavern convergence. The implementation ensures that the evolution of the pressure influences the mechanical response, which in turn feeds back into volume and pressure.

Figure 3.2 (note **u**: displacement field) illustrates the key feedback loop that links mechanical deformation with pressure loading. At each time step, the iterative solver updates the displacement field **u** until the total strain field converges within a given tolerance. In each iteration, the deformed cavern geometry is used to compute a new volume. This is passed to the pressure calculator, which updates the mean brine pressure based on compressibility. The pressure is then translated into a hydrostatic profile and applied as a Neumann boundary condition on the cavern wall.

The boundary condition is updated at every iteration within the Newton loop. This means that the system does not converge to a mechanical equilibrium, but to a coupled equilibrium where the brine pressure and deformation field are internally consistent. In the first iteration of each time step, the deformation is still zero, so the initial volume is unchanged and no pressure update occurs. In subsequent iterations, the updated displacements yield new volumes, and thus new pressures, tightening the coupling.

Once convergence is reached, the pressure, displacement, and stress fields are saved for post-processing, and the solver proceeds to the next time step. This loop continues throughout the simulation, ensuring that each mechanical step reflects the evolving fluid state inside the cavern. This dynamic update of the Neumann boundary ensures that both the mechanical and hydraulic fields evolve together in a tightly coupled, physically consistent way.

3.4. Simulation Setup

We carry out the simulations using a real-world cavern mesh provided within the SafeInCave GitLab repository [14]. This mesh, created in GMSH, represents an actual salt cavern and is used as the base geometry for all test cases. To study the impact of depth on geomechanical behavior and abandonment risks, the same cavern is placed at varying depths. For each depth scenario, simulations are repeated with hard or soft shut-in, and with and without PSC, to assess their role during long-term closure.

3.4.1. Geometry and Meshing

The cavern geometry used in all simulations is generated from a real-world design and meshed using GMSH, seen in Figure 3.3. The shape is a quarter of a vertically elongated cylindrical cavern with a slightly rounded bottom and a tapered neck at the top, reflecting realistic leaching behavior in domal salt

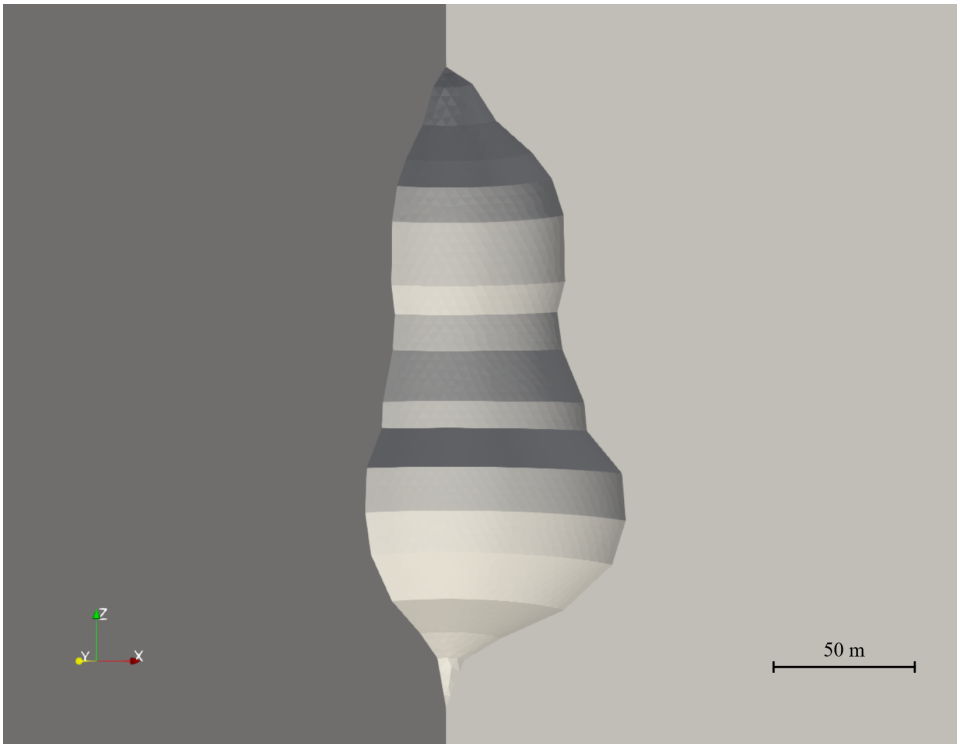

Figure 3.3: Depiction of cavern geometry.

formations. The surface mesh is tagged to allow the assignment of pressure boundary conditions along the cavern wall. The mesh itself is unstructured, made of tetrahedral elements, with local refinement near the cavern wall to better capture stress gradients and creep deformation.

The material densities used throughout the simulation are as follows.

- Salt rock: $\rho = 2,160$ kg/m^3
- Overburden: $\rho = 2,300$ kg/m^3
- Brine: $\rho = 1,168$ kg/m^3

The brine density is taken from the CoolProp database for a sodium chloride solution. Although CoolProp can express ρ_{brine} as a function of pressure, temperature, and concentration, the pressure coverage is incomplete for the range of interest, and temperature variation is not tracked in SafeInCave. Therefore, a single representative value is adopted for simplicity.

3.4.2. Boundary and Initial Conditions

The external boundaries of the domain are treated to approximate an infinite medium. The lateral boundaries are assigned roller conditions (zero normal displacement), while the bottom boundary were fully fixed. The upper surface is left free to deform vertically to allow subsidence to develop naturally.

The initial stress state is defined using lithostatic equilibrium. Vertical stress is computed from the weight of the overburden, assuming a constant density, and applied as an initial body force. No initial displacement field is imposed. The equilibrium stage allowed stress redistribution and viscoelastic prerelaxation prior to abandonment.

On the cavern wall, a 'special' Neumann boundary condition is applied to represent the brine pressure. This pressure evolved dynamically during the simulation, based on volume feedback. During equilibrium, a fixed initial pressure is used to stabilize the shape of the cavern.

Dirichlet boundary conditions were also applied to the nodes as needed to prevent rigid body motion and ensure numerical stability. These settings remained consistent across all simulation cases, regardless of the depth of the cavern or the abandonment strategy.

3.4.3. Time Stepping and Duration

Long-term abandonment simulations require efficient and stable time integration. In the early stages, small time steps are necessary to resolve rapid mechanical changes, but the abandonment period spans decades. To address this, dynamic time stepping is implemented.

SafeInCave is modified to accept either a time-step function or a list of anchor points. In our study, a series of anchor times and the corresponding desired time step sizes are defined, and a smooth mapping function is generated using PCHIP interpolation. This ensures a monotonic increase in the step size without oscillations, improving numerical stability. The primary benefit of this method is that it avoids excessively small time steps late in the simulation while still resolving early transients.

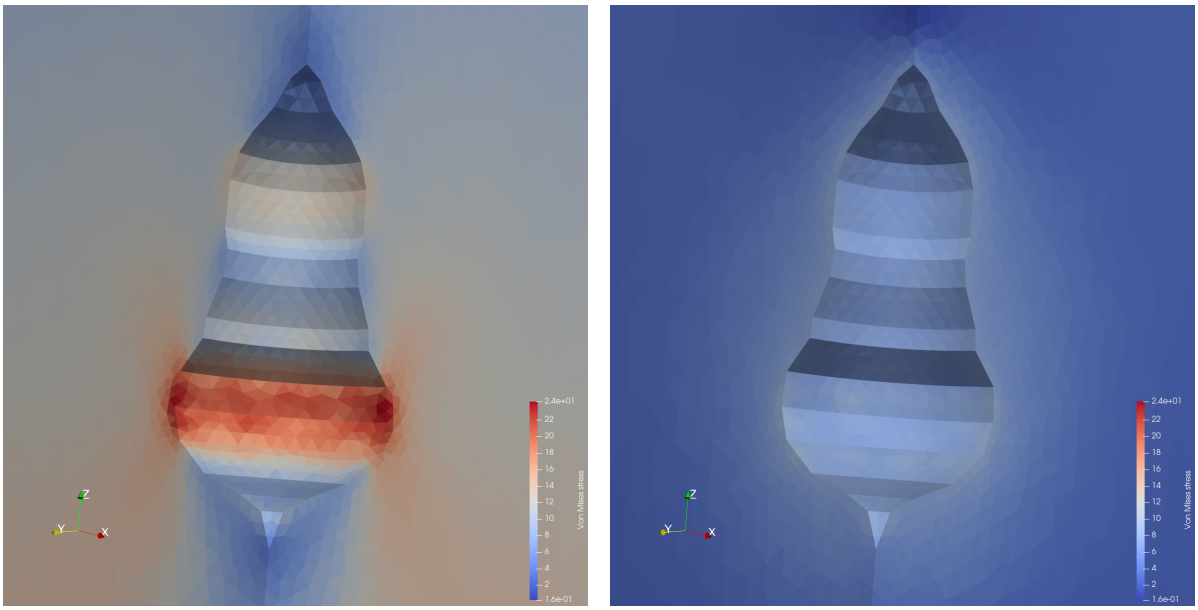

(a) (b)

Figure 3.4: Von Mises stress state evolution at start (a) and end $t_{eq} = 5$d (b) of equilibrium phase.

The equilibrium stage is run for a pseudo-time of 5 days. This was determined by visualizing stress and displacement fields in ParaView, and monitoring cavern volume over time. In all depth cases, the stress and volume evolution showed sufficient convergence by 5 days, justifying its use as a standard initialization period. Using a constant equilibrium length is important, since cavern convergence begins during equilibrium itself, see Figure 3.5. This also means that varying the length of equilibrium also has an effect on the final state of the system.

Following equilibrium, the operational (abandonment) phase is simulated for a total of 300 years. This time scale is chosen to allow the long-term features of abandonment to become apparent.

Time stepping is controlled through input anchors, with time steps ranging from 3 minutes to 4 hours for equilibrium, and 6 minutes to 500 days for abandonment. This setup allowed both short-term and long-term processes to be captured without manually tuning each step size.

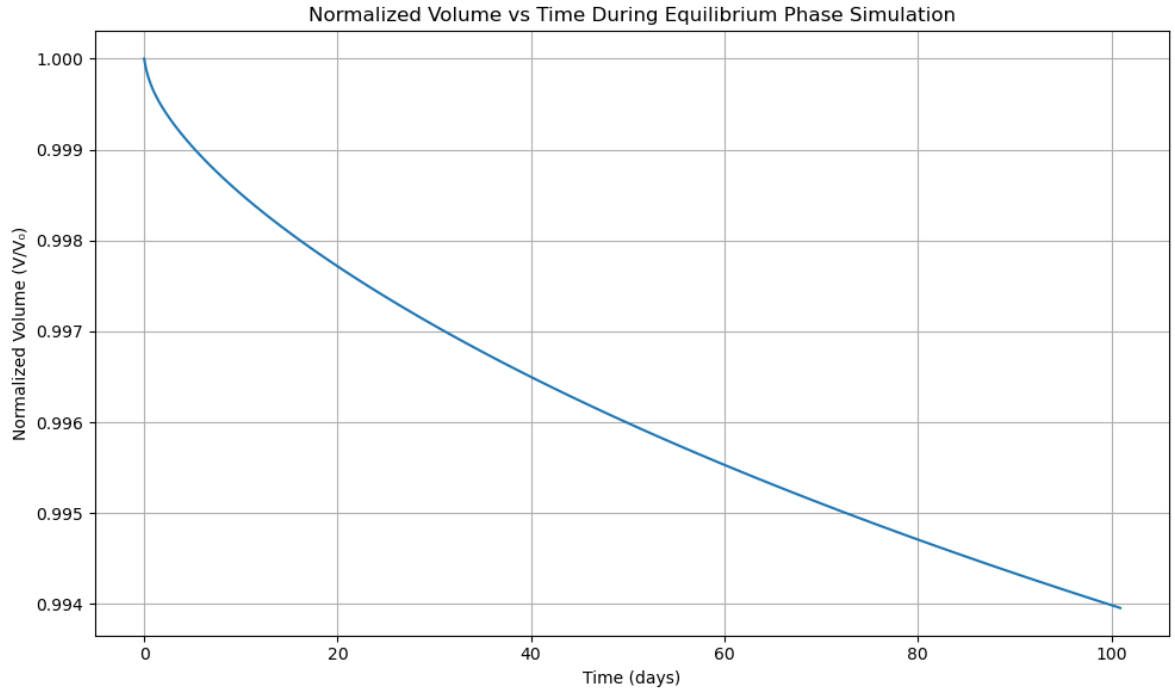

Figure 3.5: Volume over time during equilibrium phase simulations at cavern depth 800 m.

3.5. Scenarios and Parameters Tested

To evaluate the effect of different conditions on cavern behavior during abandonment, a range of simulation scenarios were constructed. Each scenario is defined by a combination of cavern depth, abandonment strategy, and whether or not PSC was included.

3.5.1. Depth Variation

The same base cavern mesh is used in all simulations, and its depth is varied to simulate different depths. The top of the cavern is placed at depths ranging from 600 m to 2200 m, in increments of 200 m resulting in nine depth scenarios. Every depth scenario consists of an overburden layer of varying thickness placed above a 1000 m thick salt layer. A hanging wall comprising 400 m of salt is situated above the cavern roof at every depth. The lithostatic pressure and thermal profile are adjusted accordingly for each case. The overburden layer is only prescribed an elastic element, while the salt layer also includes creep elements. Since creep mechanisms are sensitive to stress, this depth range was chosen to capture the transition from pressure solution creep-dominated behavior at shallow depths to dislocation creep-dominated behavior at greater depths, seen in Figure 2.1.

3.5.2. Abandonment Strategy

Two abandonment approaches are modeled:

- **Hard shut-in**: The cavern is sealed and the pressure is allowed to rise due to the compression of the brine starting from the pressure of the wellhead.
- **Soft shut-in**: The cavern is sealed at wellhead pressure. Brine is released as needed to cap the pressure at a constant value, $0.7 \cdot P_{\text{litho}}$, in line with past research [15].

Open abandonment is not considered because its use is unrealistic in practice.

3.5.3. Pressure Solution Creep Inclusion

For each depth and abandonment configuration, the simulation is run twice: once with PSC enabled and once with it disabled. This is done to isolate its effect on cavern convergence, brine-pressure evolution, and surface subsidence.

4

Results

This chapter reports on the simulation results. Section 4.1 begins with a reference run at 800 m depth, contrasting hard and soft shut-in with and without PSC. Section 4.2 repeats the experiment at depths from 600 m to 2200 m to show how depth and shut-in strategy affect pressure, volume, and subsidence. Section 4.3 then singles out the extra influence of PSC at these depths.

4.1. Fixed-Depth Simulations

To understand how the different simulation parameters affect cavern evolution and subsidence progression, four cases will first be analyzed at a fixed depth of 800 m.

4.1.1. Cavern convergence

Figure 4.1 collects the four simulations run at 800 m depth: hard and soft (70 % P_{litho}) shut-in, each with PSC included or excluded, as well as convergence rate $-d(V/V_0)/dt$.

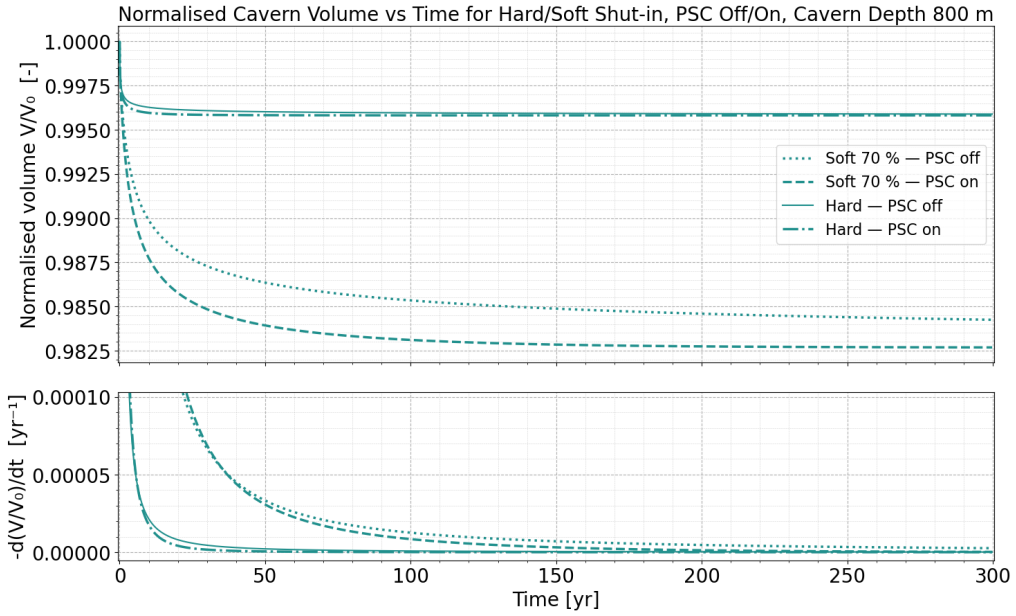

Figure 4.1: Normalized cavern volume (top) and convergence rate (bottom) during abandonment at 800 m depth

Switching on PSC reduces the final normalized volume reached in both abandonment strategies. After 300 years the hard shut-in, PSC-on case converges to a final volume slightly lower than with PSC-

off. This difference in normalized volume (0.2%) is considerably greater for soft shut-in cases, which reaches its final volume sooner. The extra loss arises from the additional volume shrinkage generated by the PSC in the salt matrix.

The PSC increment is considerably larger under soft shut-in than under hard shut-in. Since the soft cap freezes the differential stress at a still substantial level of $0.3\,P_{\mathrm{litho}}$, the PSC is able to contribute more to the total strain, whereas in hard shut-in the stress quickly decays as the pressure of the brine increases towards lithostatic pressure.

At $t = 0$, both PSC-on curves start with a steeper convergence rate. However, as soon as the brine pressure increases enough, especially for hard shut-in, the convergence rate for PSC-off overtakes after some time. Hence, with PSC-on, the final volume is reached sooner. The two rate curves then asymptotically approach one another.

Despite the rate crossover, PSC-on always retains a lower final V/V_0. The gap narrows slowly, but not fast enough, to occur within practical abandonment times.

4.1.2. Surface subsidence

Figure 4.2 plots the surface subsidence right above the centerline of the cavern for the same four 800 m cases examined in Section 4.1.1. The lower panel shows the subsidence rate.

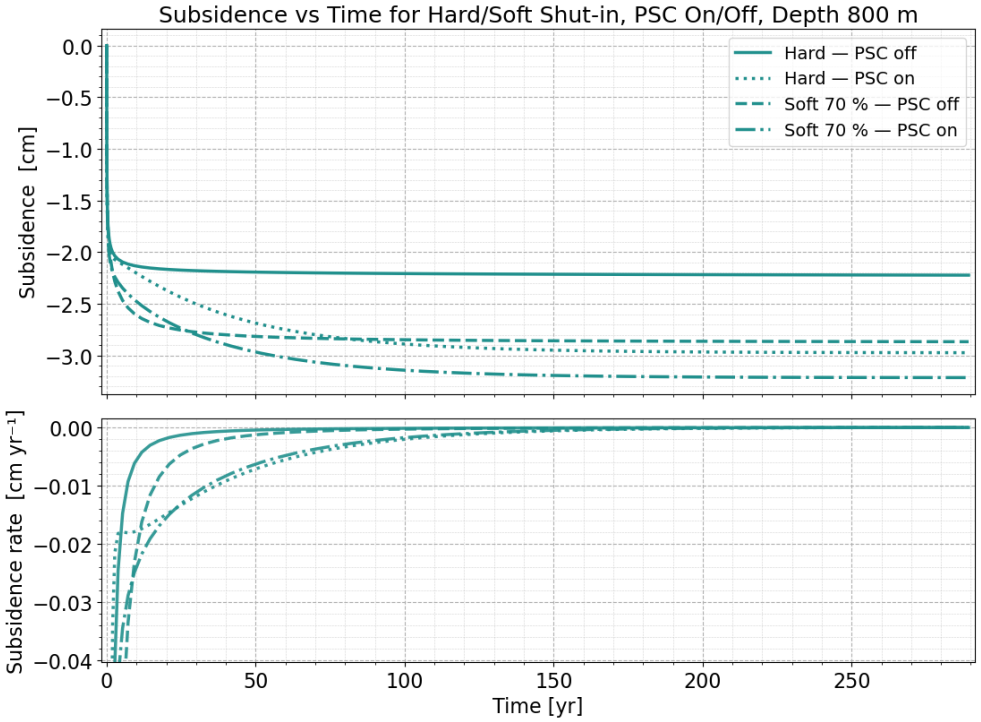

Figure 4.2: Surface subsidence (top) and rate of change (bottom) for the four parameter combinations at 800 m depth.

Turning on PSC deepens the final bowl in both pressure strategies, but the absolute increase is noticeably greater for hard shut-in (0.8 cm vs. 0.1 cm). This larger increment can be attributed to the fact that brine pressure rises closer to lithostatic pressure, causing PSC to be the dominant creep effect at this stress level with regard to subsidence.

All four curves share the same sharp downward pulse within the first year, driven by dislocation-creep closure. The PSC-on curves start with slopes nearly identical to their PSC-off counterparts, yet decay more slowly. This is because the extra volume loss from the PSC maintains a residual downward velocity. In the soft shut-in, PSC-on case, the subsidence gradient overtakes its PSC-off counterpart at $\sim$10 years, indicating a shift into a PSC-dominated regime.

Consistent with Section 4.1.1, soft shut-in produces more subsidence throughout the 300-year window, about 0.7 cm deeper than hard shut-in when PSC is deactivated, but only ∼0.4 cm deeper when PSC is active. The higher differential stress held by the soft shut-in threshold translates into higher subsidence levels in the long term.

4.2. Cavern-Depth Influence

To quantify the role of cavern depth, the following depth sweeps compare hard and soft shut-in strategies with respect to pressure build-up, cavern closure, and surface subsidence.

4.2.1. Hard Shut-in

Brine-pressure evolution

To isolate the sole effect of depth, nine simulations are run in which an identical cavern is placed vertically between 600 m and 2000 m depth and then hard shut-in at well-head pressure. Brine pressure is reported in the normalized form

$$P_{\mathrm{norm}}(t) \;=\; \frac{P_{\mathrm{brine}}(t) - P_{\mathrm{hydro}}}{P_{\mathrm{litho}} - P_{\mathrm{hydro}}}, \tag{4.1}$$

where $P_{\mathrm{hydro}} = \rho_{\mathrm{brine}} g z$ and P_{litho} is the lithostatic pressure. Thus, $P_{\mathrm{norm}} = 0$ corresponds to a fully hydrostatic column and $P_{\mathrm{norm}} = 1$ to lithostatic equilibrium.

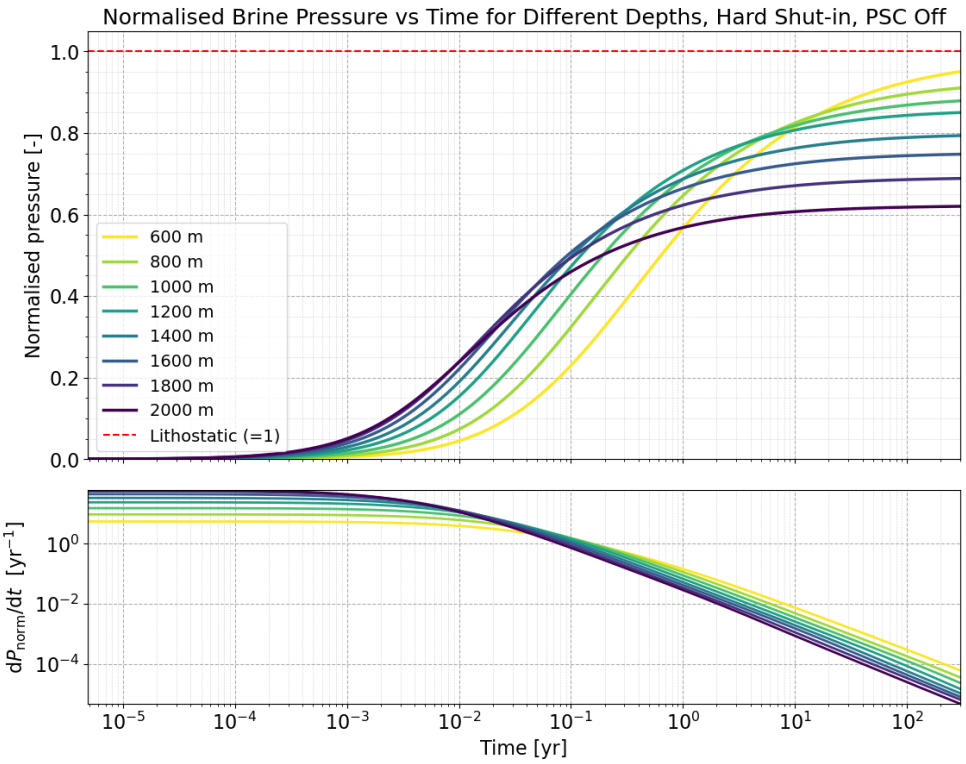

Figure 4.3: Normalized cavern pressure for depths between 0.6 km and 2.0 km under hard shut-in (PSC off) over 300 years.

Figure 4.3 shows that shallower caverns tend to approach lithostatic pressure, leveling at $P_{\mathrm{norm}} \approx 0.95$ for the 600 m case, while the deepest case plateaus at $P_{\mathrm{norm}} \approx 0.60$. Immediately after sealing, the pressure increase rate dP_{norm}/dt scales with the initial differential stress. Deeper caverns experience much higher initial pressure-increase rates, while shallower caverns show slower rates, matching shut-in tests [7]. Although deeper cavern pressures' climb fastest at first, their rate decays steeply. By time $t \approx 0.05$ years the shallower cases overtake them in the normalized pressure-gain rate. Beyond this point, shallow caverns keep closing the hydrostatic lithostatic pressure-gap, whereas deeper caverns'

rates decrease. The deeper the cavern, the farther its final pressure eventually ends up from lithostatic pressure.

Since shallow caverns come closest to lithostatic pressure, they are most susceptible to microfracturing and brine percolation once the pressure difference falls below 1 MPa.

Cavern convergence

The same depth sweep described in Section 4.2.1 is repeated, now tracking the normalized cavern volume V/V_0 over 300 years. A value of $V/V_0 = 1$ therefore denotes an undeformed cavern, while any decrease reflects mechanical closure driven by differential stress.

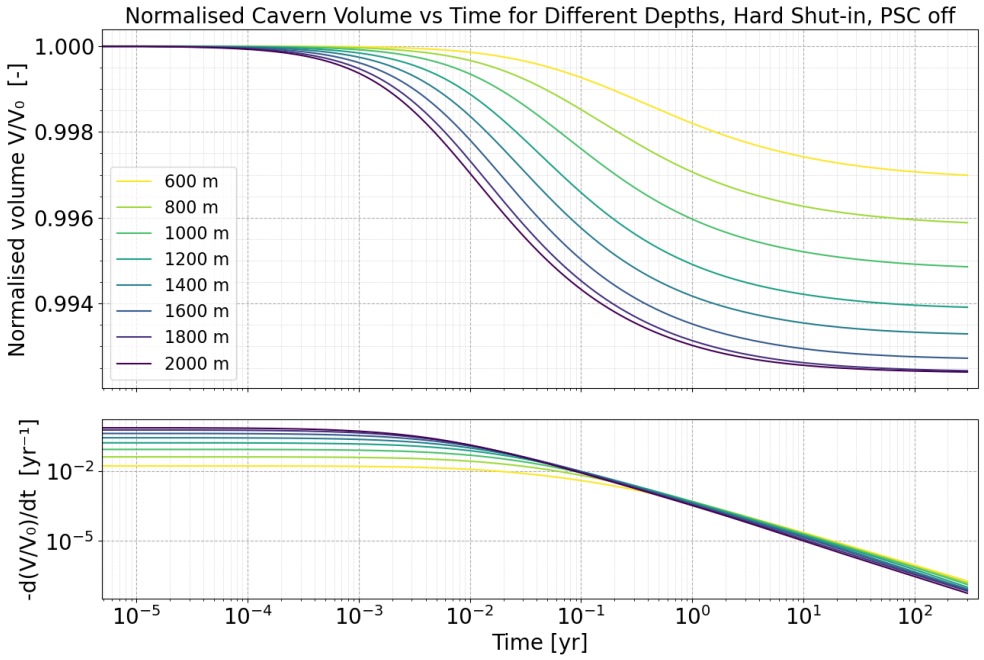

Figure 4.4: Normalised cavern volume for depths between 0.6 km and 2.0 km under hard shut-in (PSC off) over 300 years.

Figure 4.4 confirms that deeper caverns ultimately converge more. After three centuries, the 600 m cavern has lost only $\sim 0.30\,\%$ of its initial volume ($V/V_0 \approx 0.9970$), whereas the 2000 m deep case has shrunk by $\sim 0.76\,\%$ ($V/V_0 \approx 0.9924$). However, the size of these differences decreases with depth too. The geostatic load acting on deeper caverns sustains the dislocation creep for longer before the pressure feedback reduces the deviatoric stress, resulting in the observed depth trend.

Immediately after sealing, the convergence rate mirrors the pressure increase discussed in Section 4.2.1. The peak rates increase from ≈ 0.02 yr^{-1} at 600 m to ≈ 0.75 yr^{-1} at 2000 m.

Surface subsidence

Subsidence is also tracked throughout these simulations. Figure 4.5 plots the subsidence history (top) and its time-derivative (bottom) for depths 600-2000 m with PSC deactivated.

Despite experiencing the smallest convergence, the 600 m and 800 m caverns produce the deepest bowls, leveling off at 2.4 cm and 2.2 cm, respectively. The overburden acts as a mechanical filter that spreads the displacement field, and hence the thicker layers above the deep caverns damp the signal that reaches the surface.

For depths $\geq$ 1200 m, the subsidence curve shows a slight rebound: its time derivative becomes positive within the first 5-15 years, and the surface rises by up to 0.25 cm (for 2000 m depth) over the following century (Figure 4.5). This could possibly be explained by the elastic strain in the salt relaxing as the differential stress decreases, generating a small upward displacement. This effect may become more dominant as the total subsidence decreases.

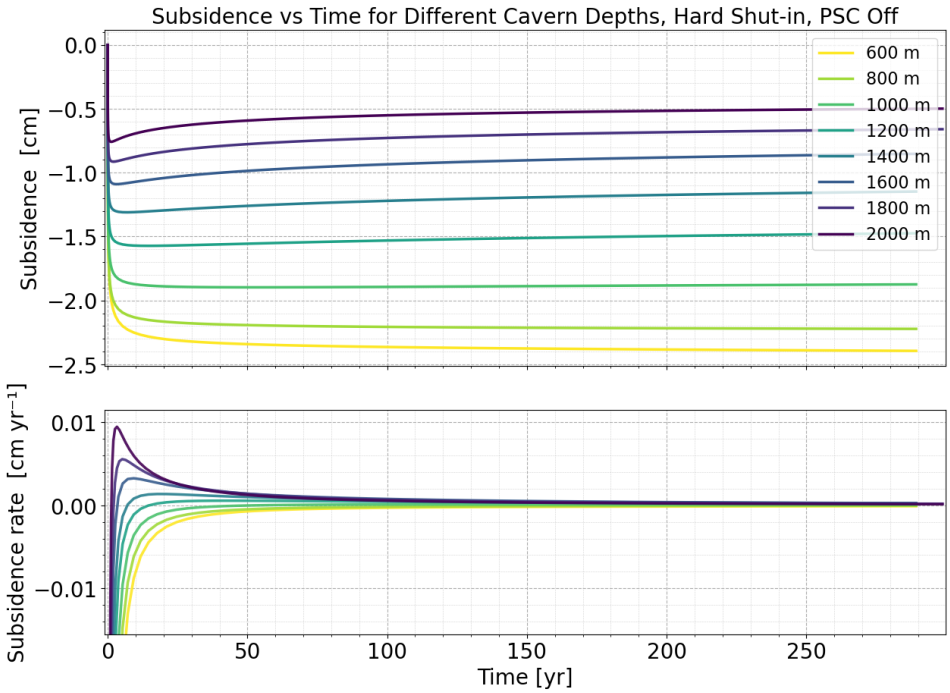

Figure 4.5: Computed surface subsidence and rate of change for hard shut-in, PSC off over 300 years, lower panel time derivative.

At $t = 0$, the shallowest caverns show the steepest rate of subsidence, whereas the deepest cases peak with the highest gradient rebound. At $t > 50$ years, all curves flatten, indicating that most measurable surface movements are restricted to the first decades after abandonment.

Stress Comparison

To understand the effect that depth has on creep, analyzing the evolution of von Mises stress q can provide further insight, as creep rates are driven by it.

In Figure 4.6(a), it can be seen that at the beginning of the simulation, the von Mises stresses are lower in the shallower cavern (800 m, left) compared to the deeper cavern (2000 m, right). However, looking at Figure 4.6(b), this situation reverses: after 300 years, the von Mises stresses end up higher in the shallower cavern than in the deeper one. Since von Mises stress drives creep, a higher convergence rate results in the deeper cavern at the start of abandonment, which is supported by Figure 4.4. The fact that shallower caverns eventually overtake deeper caverns in convergence rate, also seen in Figure 4.4, confirms that this is due to von Mises stresses in shallower caverns that eventually exceed those of deeper ones.

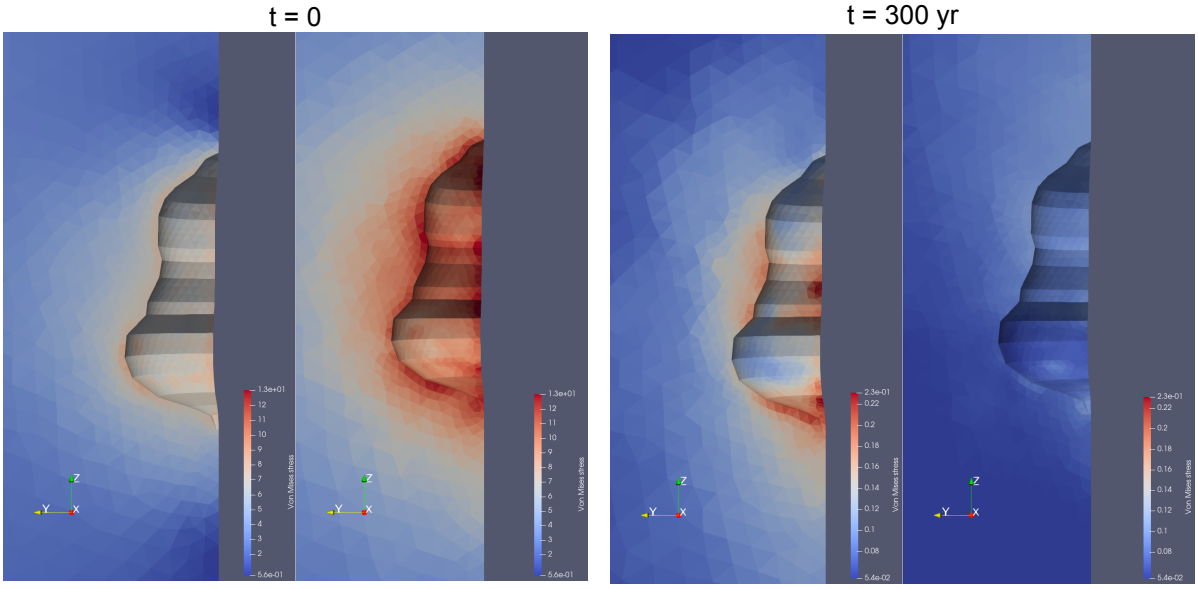

(a) Von Mises stress state at start of simulation: cavern depth 800 m (left), cavern depth 2000 m (right)

(b) Von Mises stress state after 300 years: cavern depth 800 m (left), cavern depth 2000 m (right)

Figure 4.6: Von Mises stress state evolution at start and end of abandonment phase simulation

4.2.2. Soft Shut-in

Cavern convergence

An identical depth sweep is performed with a soft shut-in strategy that limits the cavern pressure to $0.7\,P_{\mathrm{litho}}$. Figure 4.7 contrasts these runs (dotted lines) with the hard shut-in baseline (solid lines).

Unlike the hard shut-in case, total convergence is no longer strictly depth-ordered. Volume loss increases from 800 m to a maximum at 1600 m ($V/V_0 \approx 0.976$), then decreases again for depths ≥1800 m, where the 2200 m cavern ends at $V/V_0 \approx 0.983$ (Figure 4.7).

The volume curves reflect a tug-of-war between the pressure increment needed to hit the 70 % cap and the rate at which creep can generate that increment. Up to about 1600 m both factors reinforce each other: deeper caverns have a larger initial differential stress and the required pressure increment is still modest, so they reach the cap increasingly earlier. Beyond 1600 m, the required ΔP_{cap} grows faster than the creep can supply it, because every unit of closure now increases the brine pressure by a smaller fraction of P_{litho}. The cap is therefore reached later again for the 1800-2200 m cases. When the 70 % cap is reached, the differential stress is clipped to $0.3\,P_{\mathrm{litho}}$ and thereafter remains almost constant. Because steady-state creep obeys a power law with $n = 3$ for rock salt, the convergence rate at the moment of capping is “frozen in” for a period of time. Depths that reach the cap earlier do so while the instantaneous rate is still high, and therefore integrate a larger volume loss over the time that follows. Depths that reach the cap later not only spend less time in the post-cap regime but also arrive there with a lower instantaneous rate, resulting in a smaller cumulative ΔV.

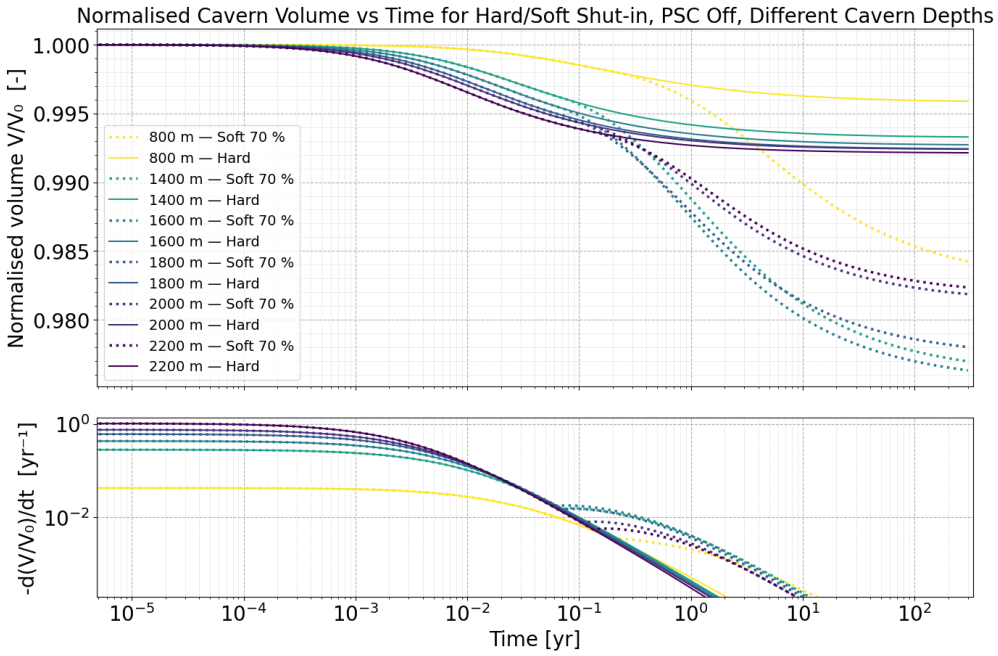

Figure 4.7: Early-time convergence for the same simulations. Top panel: V/V_0 over 300 years; bottom panel: convergence rate $-d(V/V_0)/dt$.

Surface subsidence

The subsidence can also be plotted for the soft shut-in protocol ($P_{\text{brine}} \leq 0.7\, P_{\text{litho}}$). Figure 4.8 shows the resulting surface displacement and its time derivative.

Subsidence remains strictly depth-ordered: the shallower the cavern, the larger the value. The final values range from -3.1 cm at 600 m to -0.6 cm at 2000 m. Overburden dampening therefore dominates the response even when the cavern pressure is capped. Although the caverns around the depth of 1600 m experienced the most convergence during soft shut-in, the overburden filtering effect dominates, leading to a monotonic relationship between subsidence and depth for soft shut-in. The same rebound effect seen in Figure 4.5 can be seen here.

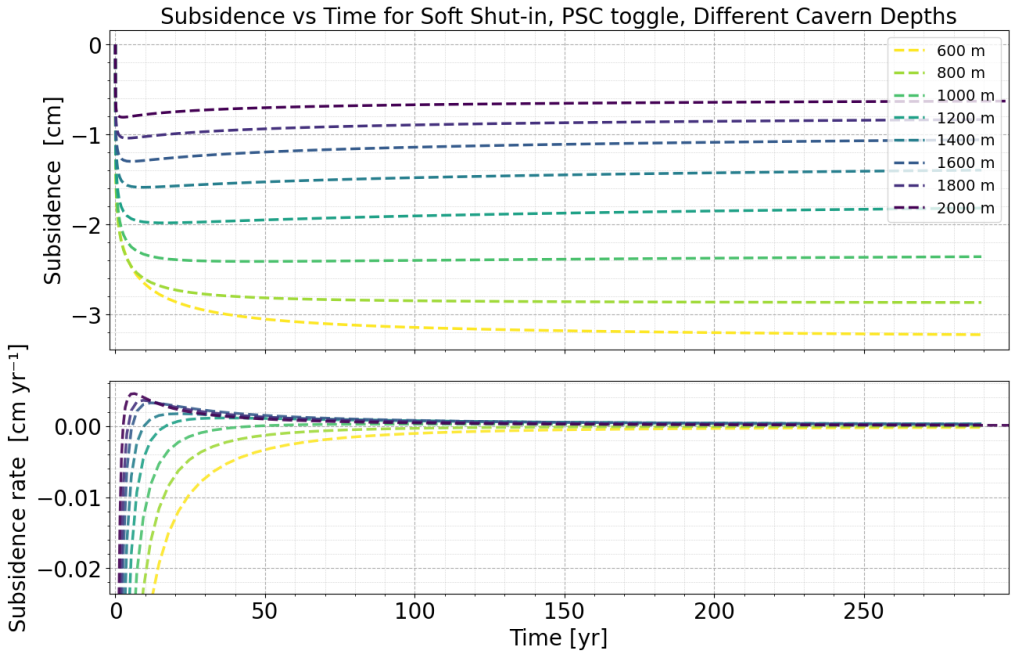

Figure 4.8: Computed surface subsidence (top) and rate of change (bottom) for soft shut-in, PSC off.

4.2.3. Hard vs. Soft shut-in: depth-wise comparison

Cavern convergence

Having presented the individual depth sweeps for hard and soft shut-in, we now place the two strategies side-by-side. Figure 4.7 already plots both data sets, now the differences will be compared.

Hard shut-in produces a clear and monotonic trend: the deeper the cavern, the greater the ultimate convergence. Under soft shut-in at 70 % lithostatic pressure, this ordering breaks down; total convergence rises from 800 m (1.6%) to a maximum (2.4% volume loss) at roughly 1600 m, then falls again for depths $\geq$1800 m (Figure 4.7). The reversal stems from the depth-dependent timing of the pressure cap: mid-depth caverns hit the threshold earliest, while their convergence rate is still high, locking in the largest long-term volume loss.

Across the entire depth range, the soft strategy ends with a greater volume loss compared to the corresponding hard shut-in case. By capping the pressure at $0.7 P_{\mathrm{litho}}$, the differential stress is never allowed to decay fully; creep, therefore, continues at a steady and slow rate for centuries. Hard shut-in, in contrast, self-limits within months once the brine pressure has climbed close enough to lithostatic pressure.

Between 1400 m and 1600 m, the gap between hard and soft shut-in outcomes peaks. This “sweet spot” corresponds to the depth at which the cap engages earliest and at the highest instantaneous convergence rate (see Figure 4.7), maximizing the lock-in effect. If minimizing cavern convergence is the primary objective, a hard shut-in remains preferable at all depths examined.

Subsidence

To gauge how the additional convergence under soft shut-in manifests itself at ground level, subsidence histories are plotted for three representative depths (800, 1400 and 2000 m), see Figure 4.9.

The shallow depths are affected most by soft shut-in. At 800 m, the final bowl deepens from -2.2 cm (hard) to -2.9 cm (soft), a 24 % increase. The extra convergence is transmitted more easily to the surface because the overburden filter is weak. The gap between hard and soft shut-in narrows with depth, but the percentage increase remains similar. At 1400 m, the difference shrinks to $\sim$0.3 cm, and by 200 m the hard and soft curves differ by less than 0.1 cm. The overburden dampening thus reduces most of the additional closure for the deep caverns.

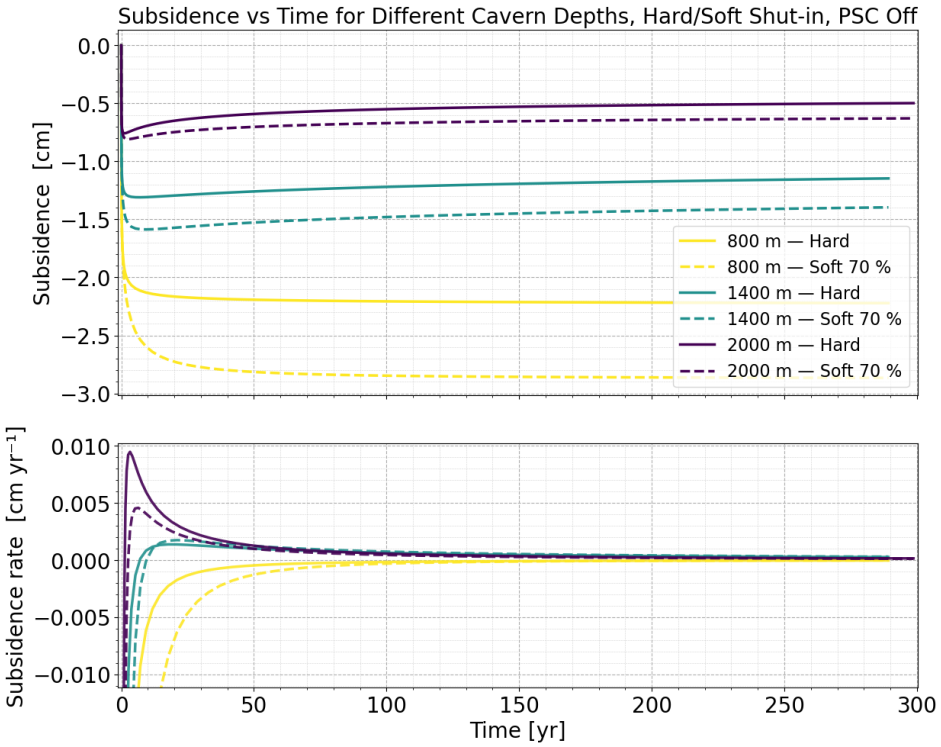

Figure 4.9: Surface subsidence for hard (solid) and soft (dashed) shut-in at three depths; PSC off. Lower panel shows the time derivative.

From a land-surface perspective, soft shut-in poses an elevated subsidence risk only for caverns shallower than ≈1 km. At greater depths, the overburden effectively masks the extra closure.

4.3. Pressure Solution Creep Effect

This section isolates and quantifies the incremental contribution of pressure□solution creep (PSC) by toggling it on/off across depths and shut-in strategies, and assesses its impact on brine-pressure build-up, cavern convergence, and surface subsidence.

4.3.1. Brine-pressure evolution

Figure 4.10 overlays PSC-on and PSC-off runs for three representative depths (800, 1400, 2000 m); all cases use hard shut-in.

PSC begins to operate as soon as differential stress exists, so every PSC-on curve rises more steeply than its PSC-off counterpart. The contribution of PSC to final pressure increases as the cavern becomes shallower and PSC's contribution to total creep increases. After 300 years, PSC still leaves a small pressure offset.

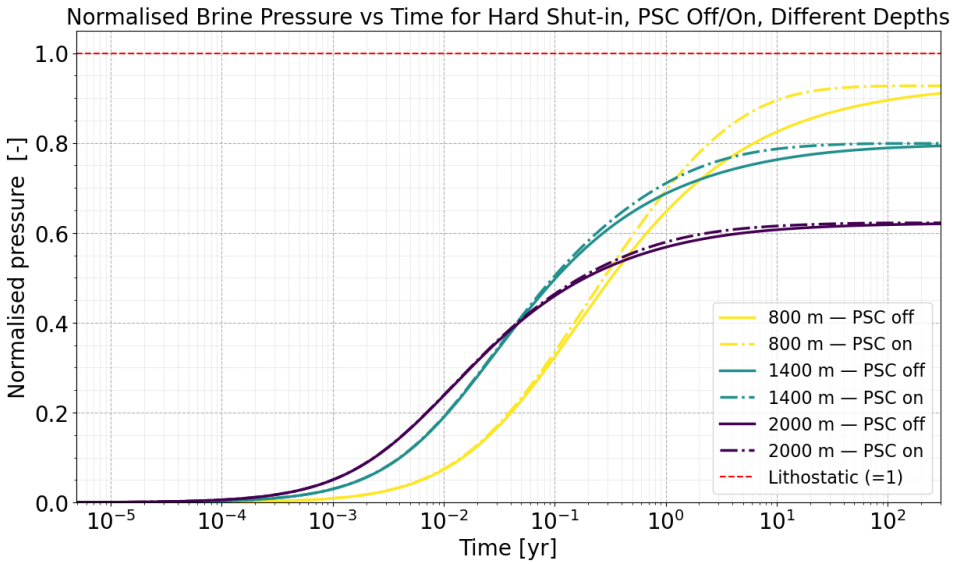

Figure 4.10: Normalised brine pressure with PSC toggled at three depths. Lithostatic pressure line ($P_{\mathrm{norm}} = 1$) added for reference.

4.3.2. Cavern convergence

Figure 4.11 overlays PSC-on and PSC-off runs for three depths under both shut-in protocols.

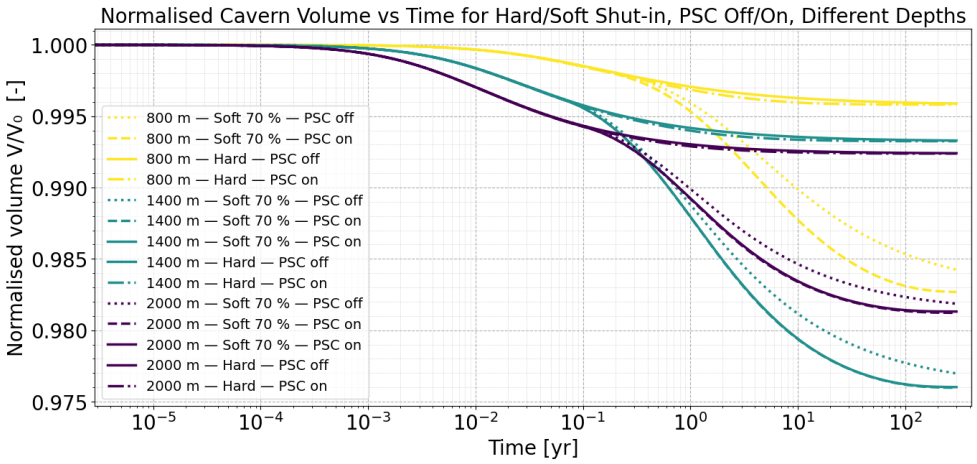

Figure 4.11: Final 300-year volume trajectories with PSC toggled at 800, 1400 and 2000 m.

For both shut-in modes, the difference between PSC enabled and disabled pairs gets smaller with depth, a sign that dislocation creep becomes the dominant effect. Although the soft shut-in 2000 m case ends with a larger absolute volume than the 1400 m case (Section 4.2.2), PSC still results in a smaller change convergence at 2000 m. The pressure cap freezes the differential stress at $0.3\,P_{\mathrm{litho}}$ and that fixed gap is a smaller driving force in MPa at a greater depth as the difference between lithostatic pressure and hydrostatic pressure expands. Hence, the incremental effect of the PSC is more governed by the magnitude of effective stress.

4.3.3. Subsidence development

Figure 4.12 shows the subsidence over time for hard shut-in with PSC activated vs deactivated at depths between 800 m and 2000 m. The corresponding soft-shut-in curves are omitted for clarity: soft shut-in resulted in <0.5 cm differences compared to hard shut-in with PSC enabled.

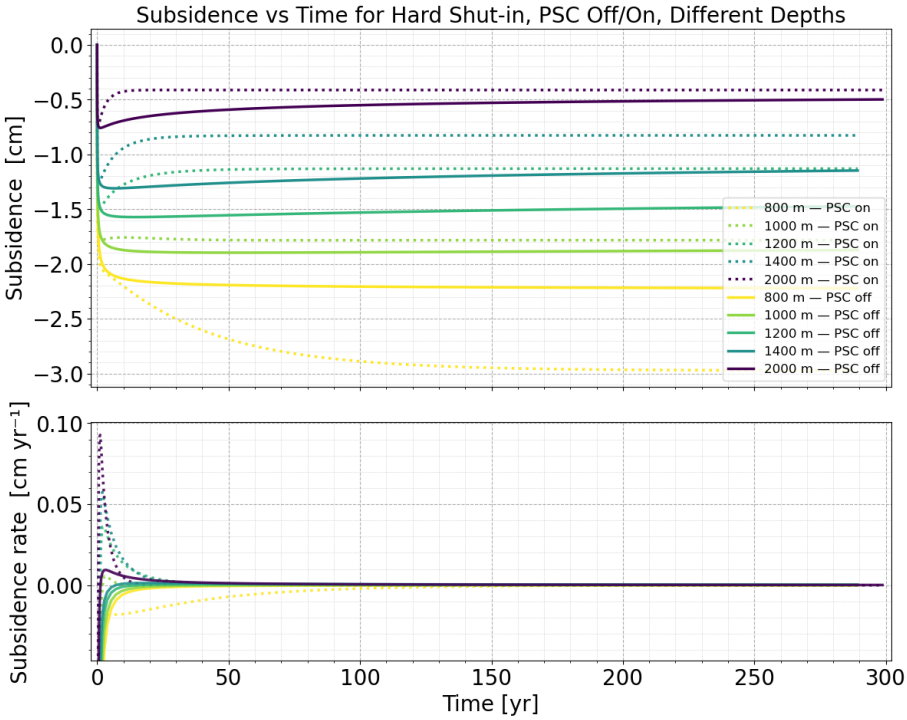

Figure 4.12: Surface subsidence (top) and rate of change (bottom) for hard shut-in with PSC toggled over 300 years

At shallow depths, the inclusion of PSC greatly affects the subsidence, increasing it by nearly 0.8 cm, a 35% increase in subsidence. However, past 1000 m depth, the inclusion of PSC leads to a subsidence *decrease* compared to the case with PSC excluded. In addition, a rebound effect becomes increasingly prominent as the depth increases.

5

Discussion

5.1. Limitations

Despite the broad parameter sweep and the brine–cavern coupling now implemented in SafeInCave, four groups of simplifying assumptions still bound the applicability of the results: the rock domain, geometry, and material properties, the constitutive laws for creep and fluid flow, and the way brine physics is represented.

Firstly, only one-quarter of the real cavern is modeled, which may bias the subsidence, particularly above the center point of the cavern. The host rock is treated as isotropic halite with depth-invariant elastic and creep parameters. Although that approximation may be more reasonable for domal salt deposits that are relatively homogeneous, it means that the impacts of bedding in bedded salt layers are not taken into account. The parameters used for the strain elements in the constitutive model (equation 3.1) were calibrated on the same salt rock sample, and it was assumed that the entire salt layer had these parameters. Therefore, the results may not be representative of the salt caverns in different salt formations, or even of the salt sample's formation itself, because of heterogeneity. This is especially true for the material parameter A_{psc}, which is dependent on grain size, and variations along a cavern can lead to different rates of convergence.

Secondly, the way the depth of the cavern was parameterized may have exaggerated the pressure offset. In the depth sweep, the cavern roof was always covered by a 400 m salt hanging wall, while the remaining distance up to ground level was assigned to the generic overburden (see Sect. 3.5.1). Consequently, each scenario was solved on a mesh whose total height and coordinate systems differed. In addition, as the overburden layer became thicker, its affect as an elastic layer became felt more, and may have resulted in allowing the cavern to deform less than it would have otherwise. To understand the effect this modeling choice had on the results, the cavern depth was also varied in a different way: having an overburden layer with constant thickness 400 m, underlain by a salt layer of thickness 2600 m and varying the position of the salt cavern in this salt layer. This lifted the normalized pressure at 2000 m from $P_{\mathrm{norm}} = 0.60$ to 0.75, but the trend (pressure deficit increasing with depth) survives (see Figure 5.1). Therefore, it could be said that the method used to vary depth in this study gives an upper bound for this effect. In addition, the rebound seen in subsidence does not occur with the altered layer geometry (see Appendix B, figure B.1). As the rebound with PSC off increased with depth (and thus overburden thickness) in the original setup, it is possible that the relatively thicker overburden layer induced this effect on the salt layer it overlays.

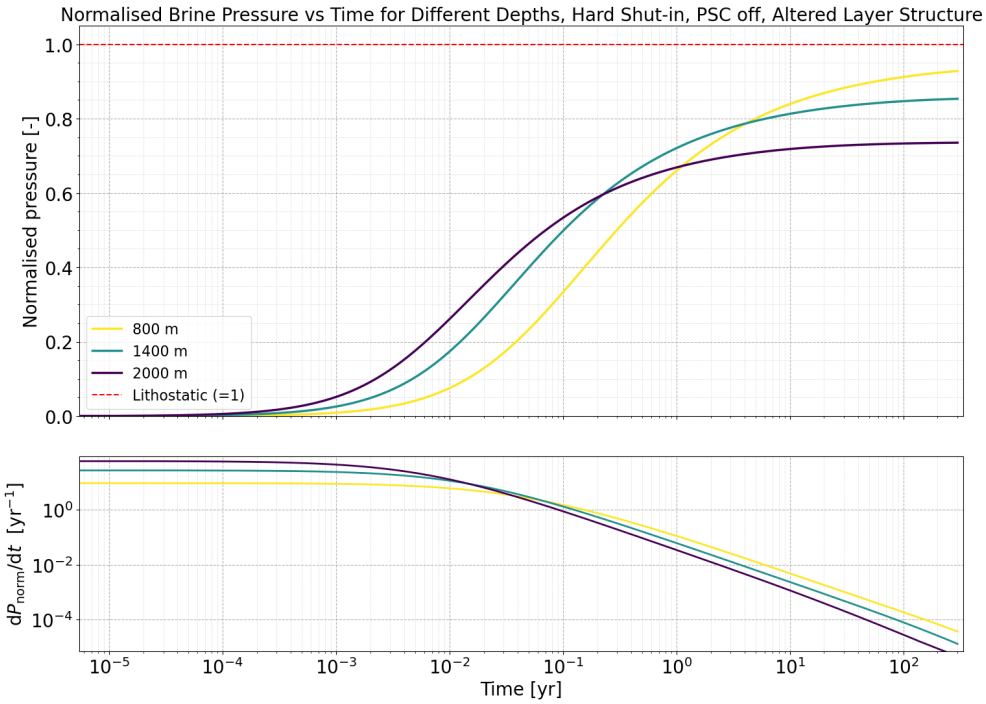

Figure 5.1: Normalized pressure plotted for hard shut-in under three cavern depths, using altered layer structuring

Third, the PSC formulation (equation 2.7) may give an upper bound value for the strain rates. It has been found that not setting a threshold stress level for PSC can lead to overpredicting the strain rates [15] and rebound in subsidence levels [22]. In the depth sweep, enabling PSC deepens the surface bowl by $\sim$0.8 cm at 800 m but actually reverses the subsidence past 1000 m depth. This rebound past 1000 m depth may be the result of the uncapped PSC element.

Lastly, brine is treated as a single isothermal phase. The simulator updates a mean cavern pressure from volume loss and then applies a depth-linear hydrostatic profile that considers the brine to have a constant density. In reality, this parameter, as well as others, can vary spatially and temporally. Including this variation could increase the accuracy of the model. Thermal expansion, percolation of the brine in the walls of the cavern, and leakage of the brine through the well are also not included in the pressure coupling. The latter is particularly relevant, because when the brine pressure gets close enough to the lithostatic pressure, microfractures form. At that point, further closure squeezes brine out of the cavern rather than raising the brine pressure above the lithostatic pressure.

6

Conclusion

6.1. Problem statement and Objectives

Salt-cavern abandonment marks the moment when active pressure control ceases and the cavern begins an evolution through a centuries-long deformation. Unchecked creep-driven convergence raises the brine pressure, redistributes stresses into the host rock, and can cause surface subsidence, fracturing, or brine percolation pathways that threaten overlying aquifers and infrastructure. Forecasting this evolution remains an open challenge, particularly for caverns marked for future hydrogen storage, where regulators require quantitative evidence that long-term risks remain within statutory bounds.

We therefore set out to answer a single guiding question: *How do abandonment strategy, cavern depth and pressure-solution creep (PSC) interact with brine-volume coupling?* The specific objectives were:

1. Extend the open-source SafeInCave simulator with code that converts each incremental loss of cavern volume into an updated hydrostatic brine pressure, closing a two-way feedback loop.
2. Run a systematic simulation series that spans a suitable range of depths. A single field-derived cylindrical mesh was placed at nine roof depths (600-2200 m, 200 m increments) and subjected to hard or soft shut-in closure strategies, with PSC included and not included.
3. Analyze features relevant to critical metrics like cavern convergence rate, brine pressure evolution, and surface subsidence.

We simulated each case to begin with a 5-day equilibrium before a 300-year abandonment phase, using spline-based adaptive time stepping to resolve early transients yet remain efficient over long timespans.

6.2. Key Findings

The set of simulations spanning nine roof depths, two abandonment strategies, and the inclusion/exclusion of PSC helped us paint a coherent picture of how salt caverns evolve once they are shut. Convergence proved restrained at the extremes: after 300 years a hard shut-in cavern at 600 m had barely lost 0.30% of its initial volume, whereas the same cavern shrunk by 0.76% at 2200 m depth. When the closure strategy was switched to soft shut-in, the spectrum widened greatly: shallow caverns lost ~1.6% of their volume while mid-depth caverns (~1600 m depth) lost 2. 4% of their volume, while the deepest case still retained 98. 4% of the original volume. Normalized brine pressure evolutions mirrored this behavior; shallow hard-shut-in caverns rose to $P \simeq 0.95 P_{litho}$ nearing the micro-fracturing threshold, whereas the 2 km case stalled near $0.6 P_{litho}$. In addition, we observed that at the start of abandonment, von Mises stress levels are higher in deep caverns, but after longer time spans, shallower caverns overtake deeper caverns in von Mises stress levels. With this information, we were able to assess the original research questions mentioned in the introduction.

Firstly, post-closure risks (RQ-1) cluster around two coupled processes: surface subsidence and near-roof overpressure leading to brine percolation. The subsidence above caverns remained gentle, <3.1

cm for the worst case (600 m, soft shut-in), and remained concentrated in the first decade of post-closure. The deeper a cavern, the less subsidence is experienced at the surface due to the filtering effect of overburden. More critically, caverns situated <1000 m deep approached the < 1 MPa threshold given for the onset of brine percolation. This suggests that brine percolation is a shallow-depth, hard shut-in problem rather than a universal closure one. The von Mises stress-level evolution we observed indicates that shallower caverns experience higher creep rates over long periods, and that this may be the reason why shallower caverns reach the brine-percolation threshold much more easily. Rebound was observed in some subsidence progressions. This behavior has been observed in previous simulation studies, which attributed the result to linear creep without threshold. This could explain the enhanced rebound observed when PSC was enabled, but not the rebound observed at higher depths when PSC is disabled. The latter could be attributed to the ever-thickening overburden layer as depth was increased.

Second, the abandonment strategy experiment (RQ-2) we performed shows that the closure strategy matters as much as depth. Hard shut-in is self-limiting: once the brine pressure creeps towards the lithostatic pressure, the vanishing differential stress slows further closure. Soft shut-in, by contrast, freezes that differential at $0.3P_{litho}$ and lets low stress-level creep continue for centuries, delivering up to three-fold more volume loss at the 1600 m 'sweet spot' and deepening the subsidence bowl above an 800 m cavern by 35%. However, after overburden filtering is accounted for, soft shut-in has a much smaller impact on subsidence at higher depths; by 2000 m depth, the hard-soft gap in subsidence is <0.1 cm. At shallower depths, soft shut-in may be necessary to ensure that the brine pressure does not get close enough to lithostatic pressure to cause brine percolation.

Third, adding PSC (RQ-3) refines and does not overturn those contrasts. PSC accelerates closure under both protocols. However, because hard shut-in rapidly drives the cavern toward lithostatic pressure, the differential stress that fuels PSC collapses after some decades, so its long-term effect on convergence is muted. Under soft shut-in, the fixed pressure offset lets low-stress PSC continue for centuries, delivering extra volume loss (more at shallower depths) compared with dislocation-creep-only runs. Enabling PSC increased subsidence by 0.8 cm at 800 m but actually had the opposite effect on subsidence past 1000 m depth, resulting in less subsidence when PSC was included. This rebound could be due to the lack of a threshold value in the PSC element.

Taken together, these findings imply that caverns whose roofs are shallower than about ~1 km develop brine pressures within ~1 MPa of lithostatic pressure under hard shut-in, a range where microfracturing and brine percolation become credible hazards. Adopting a soft shut-in cap at $0.7\,P_{\text{litho}}$ maintains the pressure margin > 5 MPa while accepting only centimeters of additional subsidence. At greater depths, cavern convergence slows due to faster reducing von Mises stress levels resulting in a lower final pressure, making deeper caverns more attractive due to their lower risk of nearing lithostatic pressure, and the overburden filtering effect that reduces the subsidence that reaches the surface.

6.3. Outlook and Future Research

We directly addressed the questions posed in Section 1.1, demonstrating how depth and shut-in strategy shape post-abandonment risks. Looking ahead, the upgraded SafeInCave model offers a solid launch pad for a more physically complete description of cavern abandonment, yet four lines of refinement stand out. First, recent research places the threshold stress for PSC between 0.07 and 0.7 MPa [15], and implementing this can reduce the excessive subsidence and rebound observed in Section 4.3.3. Second, adding brine thermal expansion, leakage and percolation to the SafeInCave simulator could allow for more realistic abandonment simulations. Allowing the brine to warm and expand after abandonment would replace the present single-phase-isothermal assumption with a coupling that captures the late-time pressure effects. Meshing the entire cavern, including asymmetric roof geometries and introducing a fracture criterion could acknowledge that micro-fracturing both creates extra storage volume and opens potential percolation pathways once the cavern pressures get close enough to the lithostatic pressure. Finally, the simulations could be rerun using the alternate layer geometry defined in Section 5.1 to reduce the effect of the thick overburden layer in deeper simulations.

In addition, interbedding is an important aspect of salt caverns that could possibly lead to cavern failure if shear stresses reach high enough levels. Preliminary runs with a 10 m layer intersecting the cavern

demonstrate that interbed composition can significantly shape long-term stability. Less-stiff claystone amplifies von Mises stress only transiently, whereas a stiff, creep-active anhydrite sustains high local von Mises stress levels throughout abandonment (more details in Appendix B.2). This contrast suggests that interbeds may control the timing and location of post-abandonment failure and therefore merit dedicated future investigation as a potential failure indicator.

Our numerical results showed that most subsidence and pressurization unfolds within the first few decades, suggesting that high-resolution monitoring during this window can serve as an early-warning system: If the measured brine pressures overshoot the model projections, the shut-in protocol can still be adjusted before the statutory thresholds are breached.

Pursuing these extensions will transform the present research tool into a decision aid capable of increasing confidence in long-term cavern abandonment regardless of whether the objective is post-mining closure or the pre-conditioning of assets for the emerging hydrogen economy.

References

[1] Mohammad Saeed Amini. “Pressure–Solution Creep Parameters for Salt”. Personal communication, 24 June 2025. Unpublished Python script and calibration dataset. 2025.

[2] J. Argyris, I. St Doltsinis, and V.D. Da Silva. “Constitutive modelling and computation of non-linear viscoelastic solids. Part I: Rheological models and numerical integration techniques”. In: *Computer Methods in Applied Mechanics and Engineering* 88.2 (July 1991), pp. 135–163. doi: 10.1016/0045-7825(91)90252-2. url: https://doi.org/10.1016/0045-7825(91)90252-2.

[3] E. Arrospide et al. *Mechanical properties of polymer-optical fibres*. Sept. 2016, pp. 201–216. doi: 10.1016/b978-0-08-100039-7.00007-5. url: https://doi.org/10.1016/b978-0-08-100039-7.00007-5.

[4] General Project Management BECi and Sub Surface Design. *Update Subsidence Analysis & Forecast.final: Based on Levelling Survey Oct 2003*. Tech. rep. Approved by Dr. H.J. Barge (Managing Director FRISIA); Agreed by L. Mulder, T.W. Bakker, and D. van Tuinen. The Netherlands: FRISIA, Dec. 2003.

[5] Ian H. Bell et al. “Pure and Pseudo-pure Fluid Thermophysical Property Evaluation and the Open-Source Thermophysical Property Library CoolProp”. In: *Industrial & Engineering Chemistry Research* 53.6 (2014), pp. 2498–2508. doi: 10.1021/ie4033999. eprint: http://pubs.acs.org/doi/pdf/10.1021/ie4033999. url: http://pubs.acs.org/doi/abs/10.1021/ie4033999.

[6] J.N. Breunese et al. “Observation and prediction of the relation between salt creep and land subsidence in solution mining. The Barradeel Case”. In: *Proceedings of the Solution Mining Research Institute Fall Meeting*. Chester, 2003.

[7] B. Brouard, P. Bérest, and M. Karimi-Jafari. *Deep salt-cavern abandonment*. Dec. 2017, pp. 445–452. doi: 10.1201/9781315106502-53. url: https://doi.org/10.1201/9781315106502-53.

[8] Michael S. Bruno and Maurice B. Dusseault. “Geomechanical Analysis of Pressure Limits for Thin Bedded Salt Caverns”. In: *Solution Mining Research Institute, Spring 2002 Technical Meeting* (2002). url: https://www.terralog.com/article/smri.pdf.

[9] René Buzogany et al. *Development of surface deformations above salt caverns depending on the abandonment scenario*. June 2022, pp. 553–566. doi: 10.1201/9781003295808-51. url: https://doi.org/10.1201/9781003295808-51.

[10] D. Dorner, K. Röller, and B. Stöckhert. “High temperature indentation creep tests on anhydrite – a promising first look”. In: *Solid Earth* 5.2 (Aug. 2014), pp. 805–819. doi: 10.5194/se-5-805-2014. url: https://doi.org/10.5194/se-5-805-2014.

[11] Hermínio T. Honório and Hadi Hajibeygi. *SafeInCave 1.0.0 - User Manual*. Accessed from internal TU Delft project repository. TU Delft – Civil Engineering and Geosciences. 2023.

[12] Hermínio T. Honório and Hadi Hajibeygi. “Three-dimensional multi-physics simulation and sensitivity analysis of cyclic energy storage in salt caverns”. In: *International Journal of Hydrogen Energy* 94 (Nov. 2024), pp. 1389–1405. doi: 10.1016/j.ijhydene.2024.11.081. url: https://doi.org/10.1016/j.ijhydene.2024.11.081.

[13] Hermínio T. Honório et al. “A multi-step calibration strategy for reliable parameter determination of salt rock mechanics constitutive models”. In: *International Journal of Rock Mechanics and Mining Sciences* 183 (Sept. 2024), p. 105922. doi: 10.1016/j.ijrmms.2024.105922. url: https://doi.org/10.1016/j.ijrmms.2024.105922.

[14] Hermínio Tasinafo Honório. *ADMIRE*$_{Public/SafeInCaveGitLab}$. url: https://gitlab.tudelft.nl/ADMIRE_Public/safeincave.

[15] Luuk Hunfeld, Jaap Breunese, and Brecht Wassing. *The influence of a threshold stress for pressure solution creep on cavern convergence and subsidence behavior – An FEM study*. June 2022, pp. 577–589. doi: 10.1201/9781003295808-53. url: https://doi.org/10.1201/9781003295808-53.

[16] Martin P. A. Jackson and Michael R. Hudec. *Salt tectonics*. Cambridge University Press, Feb. 2017.

[17] Kavan Khaledi et al. "Stability and serviceability of underground energy storage caverns in rock salt subjected to mechanical cyclic loading". In: *International Journal of Rock Mechanics and Mining Sciences* 86 (Apr. 2016), pp. 115–131. doi: 10.1016/j.ijrmms.2016.04.010. url: https://doi.org/10.1016/j.ijrmms.2016.04.010.

[18] Kishan Ramesh Kumar et al. "Comprehensive review of geomechanics of underground hydrogen storage in depleted reservoirs and salt caverns". In: *Journal of Energy Storage* 73 (Sept. 2023), p. 108912. doi: 10.1016/j.est.2023.108912. url: https://doi.org/10.1016/j.est.2023.108912.

[19] Kishan Ramesh Kumar et al. "Geomechanical simulation of energy storage in salt formations". In: *Scientific Reports* 11.1 (Oct. 2021). doi: 10.1038/s41598-021-99161-8. url: https://doi.org/10.1038/s41598-021-99161-8.

[20] Muath Al Malki et al. "In situ observation of electrical resistivity increase via creep-induced dislocations in n-type PbTe". In: *Acta Materialia* 266 (Jan. 2024), p. 119652. doi: 10.1016/j.actamat.2024.119652. url: https://doi.org/10.1016/j.actamat.2024.119652.

[21] Piotr Małkowski, Łukasz Ostrowski, and Jarosław Brodny. "Analysis of Young's modulus for Carboniferous sedimentary rocks and its relationship with uniaxial compressive strength using different methods of modulus determination". In: *Journal of Sustainable Mining* 17.3 (Jan. 2018), pp. 145–157. doi: 10.1016/j.jsm.2018.07.002. url: https://doi.org/10.1016/j.jsm.2018.07.002.

[22] G. Marketos, C. J. Spiers, and R. Govers. "Impact of rock salt creep law choice on subsidence calculations for hydrocarbon reservoirs overlain by evaporite caprocks". In: *Journal of Geophysical Research Solid Earth* 121.6 (June 2016), pp. 4249–4267. doi: 10.1002/2016jb012892. url: https://doi.org/10.1002/2016jb012892.

[23] Joseph Martinez, Kenneth Johnson, and James Neal. "Sinkholes in evaporite rocks". In: *American Scientist* 86.1 (Jan. 1998), p. 38. doi: 10.1511/1998.1.38. url: https://doi.org/10.1511/1998.1.38.

[24] Jean Donald Minougou, Raoof Gholami, and Pål Andersen. "Underground hydrogen storage in caverns: Challenges of impure salt structures". In: *Earth-Science Reviews* 247 (Oct. 2023), p. 104599. doi: 10.1016/j.earscirev.2023.104599. url: https://doi.org/10.1016/j.earscirev.2023.104599.

[25] Oscar Molina, Victor Vilarrasa, and Mehdi Zeidouni. "Geologic carbon storage for shale gas recovery". In: *Energy Procedia* 114 (July 2017), pp. 5748–5760. doi: 10.1016/j.egypro.2017.03.1713. url: https://doi.org/10.1016/j.egypro.2017.03.1713.

[26] C. J. Spiers et al. "Experimental determination of constitutive parameters governing creep of rocksalt by pressure solution". In: *Geological Society London Special Publications* 54.1 (Jan. 1990), pp. 215–227. doi: 10.1144/gsl.sp.1990.054.01.21. url: https://doi.org/10.1144/gsl.sp.1990.054.01.21.

[27] J.L. Urai and C.J. Spiers. *The effect of grain boundary water on deformation mechanisms and rheology of rocksalt during long-term deformation*. Dec. 2017, pp. 149–158. doi: 10.1201/9781315106502-17. url: https://doi.org/10.1201/9781315106502-17.

[28] Reinier Van Noort, Hendrica J. M. Visser, and Christopher J. Spiers. "Influence of grain boundary structure on dissolution controlled pressure solution and retarding effects of grain boundary healing". In: *Journal of Geophysical Research Atmospheres* 113.B3 (Feb. 2008). doi: 10.1029/2007jb005223. url: https://doi.org/10.1029/2007jb005223.

[29] Chunhe Yang, J.J.K. Daemen, and Jian-Hua Yin. “Experimental investigation of creep behavior of salt rock”. In: *International Journal of Rock Mechanics and Mining Sciences* 36.2 (Feb. 1999), pp. 233–242. doi: 10.1016/s0148-9062(98)00187-9. url: https://doi.org/10.1016/s0148-9062(98)00187-9.

[30] Guimin Zhang et al. “Ground subsidence Prediction Model and parameter Analysis for underground gas storage in horizontal salt caverns”. In: *Mathematical Problems in Engineering* 2021 (Sept. 2021), pp. 1–16. doi: 10.1155/2021/9504289. url: https://doi.org/10.1155/2021/9504289.

[31] H. W. Zhou et al. “A fractional derivative approach to full creep regions in salt rock”. In: *Mechanics of Time-Dependent Materials* 17.3 (Sept. 2012), pp. 413–425. doi: 10.1007/s11043-012-9193-x. url: https://doi.org/10.1007/s11043-012-9193-x.

A

Source Code

A.1. Brine-Cavern Coupling Code

Listings A.1.1 and A.1.2 form the volume-pressure feedback loop in SafeInCave: the first computes and tracks cavern volume in a class, the second calls this class to facilitate the brine-pressure coupling. Supporting code is not included. For the full simulator code, please see visit our GitLab Repository.

A.1.1. VolumeMonitor.py

Extracts the cavern surface, orients the facets, and, after every Newton step, logs the updated volume and mean brine pressure via the divergence theorem and an isothermal compressibility law.

```
"""
VolumeMonitor class for tracking the volume of a cavern surface as well as computing pressure change in a simulation
This module provides functionality to compute the volume of a cavern surface, track changes over time, and calculate pressure changes in brine using the CoolProp library.
It includes methods for extracting surface data from a GMSH grid, calculating centroids, orienting triangles, and computing volumes using the divergence theorem.
"""

from dolfin import *
import numpy as np
import sys
import os
import Utils as utils
sys.path.append("./safeincave")
from Grid import GridHandlerGMSH
from CoolProp.CoolProp import PropsSI



def compute_pressure_change(vol_t0, vol_t1, temperature=300, pressure=101325, fluid="INCOMP::MNA[0.30]"): ## new entire function, CoolProp part
    """Calculate pressure change in brine using CoolProp."""
    compressiblity = PropsSI("ISOTHERMAL_COMPRESSIBILITY", "P", pressure, "T", temperature, "Water") #Takes comprssibility of water at given temperature and pressure
    density = PropsSI("D", "P", pressure, "T", temperature, fluid)  # Density of brine at given conditions (kg/m³)
    delta_V = abs(vol_t1 - vol_t0)  # Volume change (m³)
    delta_P = (1/compressiblity) * np.log(vol_t0/vol_t1)  # Pressure change (Pa)
    return delta_P, density


def extract_cavern_surface_from_grid(grid: GridHandlerGMSH, boundary_name: str):
    """Extracts the coordinates and triangles of a cavern surface from a GMSH grid."""
    mesh = grid.mesh
    facet_function = grid.get_boundaries()
    boundary_id = grid.get_boundary_tags(boundary_name)
    coordinates = mesh.coordinates()
```

```
33
34      # Extract triangles
35      triangles = []
36      for facet in facets(mesh):
37          if facet_function[facet.index()] == boundary_id:
38              triangle = [vertex.index() for vertex in vertices(facet)]
39              if len(triangle) == 3:
40                  triangles.append(triangle)
41      return np.array(coordinates), np.array(triangles, dtype=np.int32)
42
43
44  def surface_centroid(coordinates, triangles):
45      """Calculate the centroid of a surface defined by triangles."""
46      total_area = 0
47      weighted_sum = np.zeros(3)
48      for tri in triangles:
49          p0, p1, p2 = coordinates[tri]
50          center = (p0 + p1 + p2) / 3.0
51          area = np.linalg.norm(np.cross(p1 - p0, p2 - p0)) / 2.0
52          weighted_sum += center * area
53          total_area += area
54      return weighted_sum / total_area
55
56  def orient_triangles_outward(coordinates, triangles, reference_point):
57      """Orient triangles so that their normals point outward from a reference point."""
58      fixed_triangles = []
59      for tri in triangles:
60          p0, p1, p2 = coordinates[tri]
61          normal = np.cross(p1 - p0, p2 - p0)
62          center = (p0 + p1 + p2) / 3.0
63          inward = reference_point - center
64          if np.dot(normal, inward) > 0:
65              fixed_triangles.append([tri[0], tri[2], tri[1]])
66          else:
67              fixed_triangles.append(tri)
68      return np.array(fixed_triangles)
69
70  def compute_volume(coordinates, triangles):
71      """Calculate the volume of a closed surface defined by triangles using the divergence
            theorem."""
72      centroid= surface_centroid(coordinates, triangles)
73      volume = 0
74      for triangle in triangles:
75          v0 = coordinates[triangle[0]] - centroid
76          v1 = coordinates[triangle[1]] - centroid
77          v2 = coordinates[triangle[2]] - centroid
78          volume += np.dot(v0, np.cross(v1, v2)) / 6.0
79      return volume
80
81
82  def cavern_top_bottom(coords_def, tris, direction=2):
83      """Determine the top and bottom z-coordinates of the cavern wall."""
84      wall_ind = np.unique(tris.ravel())
85      z_wall   = coords_def[wall_ind, direction]
86      return z_wall.max(), z_wall.min()
87
88  class VolumeMonitor:
89      """
90      Computes the deformed volume of a closed surface at *every* pseudo-time step.
91      """
92      def __init__(self, grid: GridHandlerGMSH, boundary_name: str = "Cavern"):
93          self.coords0, tris = extract_cavern_surface_from_grid(grid, boundary_name)
94          ctr = surface_centroid(self.coords0, tris)
95          reference_point = np.array([0, 0, ctr[2]])
96          self.tris = orient_triangles_outward(self.coords0, tris, ctr)
97          self.mesh = grid.mesh
98          self.time, self.volume, self.pressure = [], [], []
99
100     def record_0(self,t, u, p=None):
101         """Append volume at time *t* given the current displacement field *u*."""
102         self.time.append(float(t))
```

```
        disp = u.compute_vertex_values(self.mesh).reshape(3, -1).T
        self.volume.append(float(compute_volume(self.coords0 + disp, self.tris)))
        if p is not None:
            self.pressure.append(float(p))

    def record(self, u: Function, t, p):
        """Append volume at time *t* given the current displacement field *u*."""
        disp = u.compute_vertex_values(self.mesh).reshape(3, -1).T
        coords_def = self.coords0 + disp
        z_top, z_bottom = cavern_top_bottom(coords_def, self.tris)
        self.time.append(float(t))
        self.volume.append(float(compute_volume(coords_def, self.tris)))
        self.pressure.append(float(p))

    def dump(self, folder, simulation_name=None):
        fname = f"volume_{simulation_name}.json" if simulation_name else "volume.json"
        os.makedirs(folder, exist_ok=True)
        utils.save_json(
            {"time": self.time,
            "volume": self.volume,
            "pressure": self.pressure},
            os.path.join(folder, fname))
```

A.1.2. Brine Pressure BC coupling

Updates the Neumann load as $P(z) = P_{\text{top}} - \rho g(z_{\text{top}} - z)$ each iteration, applies an optional shut-in cap, and keeps the mechanics and fluid states in sync.

```
def apply_special_neumann_bc(self, t=None): #incorporate self.tris, self.coords0 . Also incorporate volume initializer
    """

    """

    self.integral_special_neumann = []
    i = 0
    bc_neumann_list = []
    for boundary in self.input_file["boundary_conditions"]:
        if self.input_file["boundary_conditions"][boundary]["type"] == "special_neumann":
            # Read boundary condition parameters
            bc_direction = self.input_file["boundary_conditions"][boundary]["direction"]
            rho_brine = self.input_file["boundary_conditions"][boundary]["density"]
            ref_position = self.input_file["boundary_conditions"][boundary]["
                reference_position"]
            g = abs(self.gravity)

            # Compute current deformed coordinates, top and bottom of cavern, and volume
            disp = self.u.compute_vertex_values(self.grid.mesh).reshape(3, -1).T
            coords_def = self.coords0 + disp
            z_top, z_bottom = cavern_top_bottom(coords_def, self.tris, direction=bc_direction
                )
            V_t1_k = compute_volume(coords_def, self.tris)

            # Initializes Volume, only true for first iteration of first time step
            if self.V_t0 is None:
                P_0 = self.input_file["boundary_conditions"][boundary]["P_0"]
                self.P_top = P_0
                self.P_bot = P_0 + rho_brine * g * abs(z_top-z_bottom)
                self.P_t0 = 0.5*(self.P_top + self.P_bot)
                self.stress_monitor.record(0, self.stress_torch, self.P_top, self.P_bot)
                self.volume_monitor.record_0(0, self.u, p=self.P_t0)
                self.V_t0 = self.volume_monitor.volume[0]
            else:
                self.P_t0 = self.volume_monitor.pressure[-1]
                self.V_t0 = self.volume_monitor.volume[-1]

            # Calculate pressure change and new mean pressure, converts to top and bottom
                pressure
            delta_P_t1_k, rho_brine_t1  = compute_pressure_change(self.V_t0, V_t1_k,
                temperature=300, pressure=self.P_t0, fluid="INCOMP::MNA[0.230]")
            P_t1_k  = self.P_t0 + delta_P_t1_k
```

```
            self.P_top = P_t1_k - rho_brine * g * abs((z_top-z_bottom)/2)
            self.P_bot = P_t1_k + rho_brine * g * abs((z_top-z_bottom)/2)

            # Implements soft shut-in pressure threshold if prescribed
            if self.input_file["boundary_conditions"][boundary]["P_threshold"] is not None:
                P_threshold = self.input_file["boundary_conditions"][boundary]["P_threshold"]
                if self.P_top < P_threshold:
                    self.P_top = self.P_top
                else:
                    self.P_top = P_threshold
                    P_t1_k = self.P_top + rho_brine * g * abs((z_top-z_bottom)/2)
                    self.P_bot = self.P_top + rho_brine * g * abs((z_top-z_bottom))
                    print(f"Pressure threshold reached at boundary {boundary}. Pressure set
                        to {P_threshold/1e6} MPa.")


            self.P_iter = P_t1_k        # store for next iteration
            value_special_neumann = do.Expression(f"load_ref - rho*g*(H - x[{bc_direction}])"
                , load_ref = -self.P_top, rho=rho_brine , g = abs(self.gravity), H = z_top,
                degree = 1)
            self.integral_special_neumann.append(value_special_neumann*self.normal*self.ds(
                self.grid.get_boundary_tags(boundary)))
```

B

Supporting Material

B.1. Subsidence plot for altered layer geometry

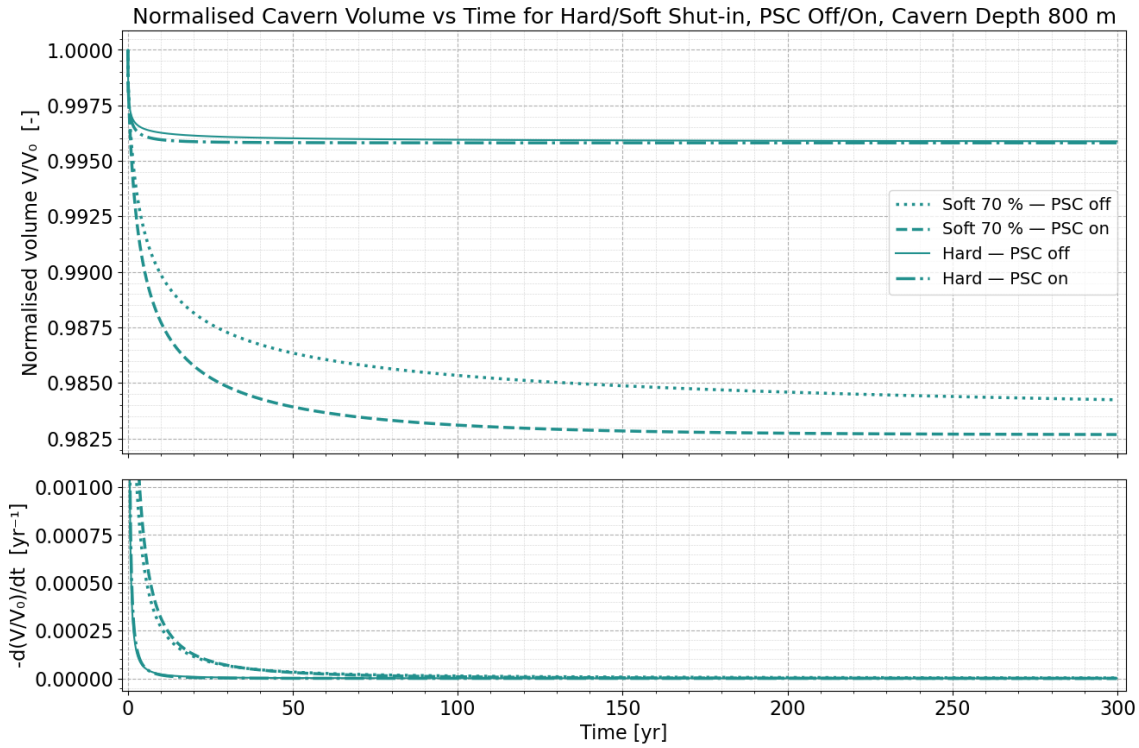

Figure B.1: Subsidence plot for the altered layer geometry

B.2. Interlayer Analysis

To quantify the influence of an interbed on cavern abandonment behaviour, a 10 m thick layer was inserted at mid-height of the salt layer so that it intersected the cavern walls. The time evolution of the von Mises equivalent stress, q, was taken as an indicator for shear-failure potential: a sustained rise in q can precede bed-plane slip and possibly the loss of cavern integrity.

Two different layer compositions were modelled: Claystone with $E = 8\ \mathrm{GPa}$ [21] and no dislocation creep element [18], and anhydrite with $E = 68\,\mathrm{GPa}$ and dislocation creep parameters $Q = 338\,\mathrm{kJ\,mol^{-1}}$, $n = 3.9$, and $A = 4.8 \times 10^{-19}\ \mathrm{Pa^{-3.9}\,s^{-1}}$ [10].

Immediately after the equilibrium phase ($t = 0$) the claystone case exhibited lower q levels than the anhydrite case (Figure B.2).

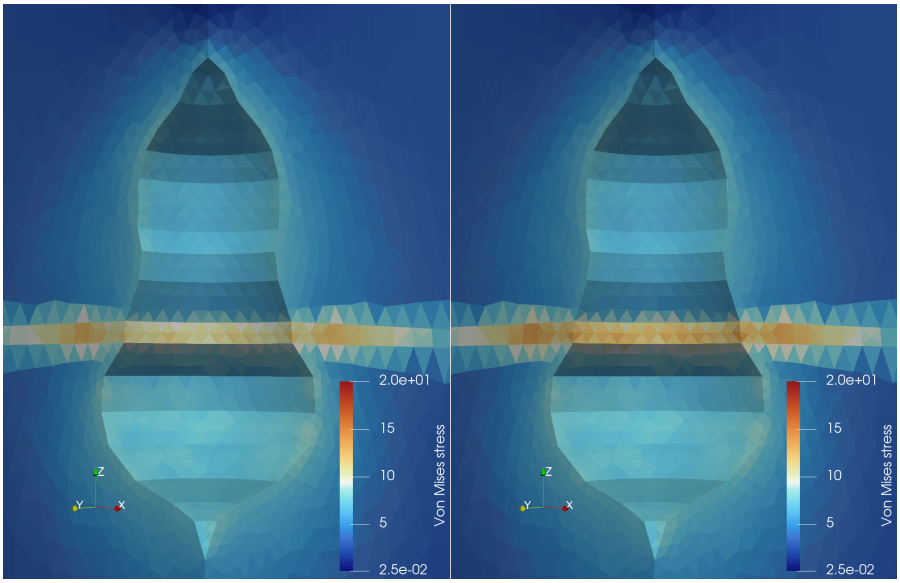

Figure B.2: Von Mises equivalent stress at t=0 for the interbed runs: claystone interbed (left) versus anhydrite interbed (right).

As abandonment progressed, stress in the surrounding salt relaxed, while q within both interbeds rose.

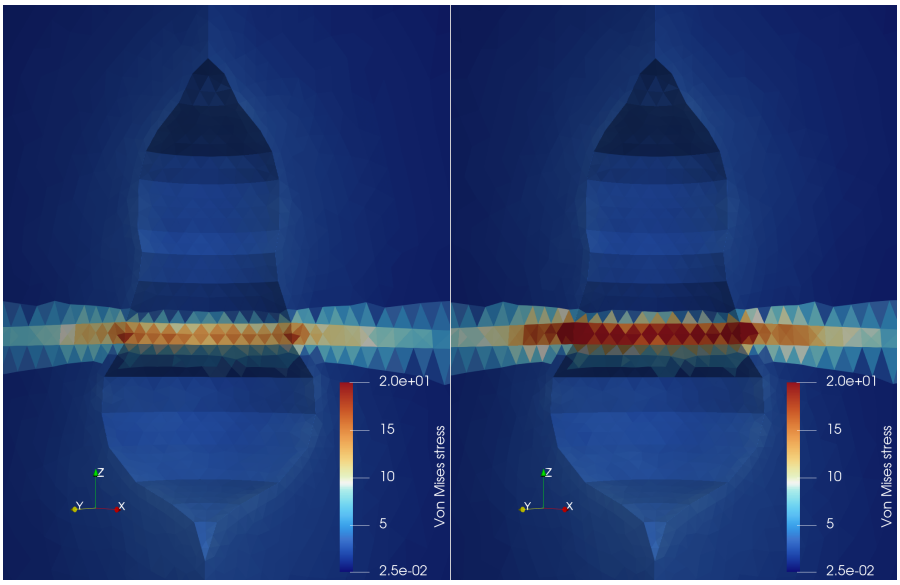

Figure B.3: Von Mises equivalent stress at t=100 days for the interbed runs: claystone interbed (left) versus anhydrite interbed (right).

The claystone and anhydrite layers both reached their peak stress levels at $t = 100$d (see Figure B.3) after which the claystone layer's stresses decayed, approaching the rest of the cavern-wall level after roughly one century. By contrast, the anhydrite retained elevated stresses: local q pockets remained near 20 MPa, indicating a prolonged concentration of shear load within the stiffer layer with dislocation creep (see Figure B.4).

These trends suggest that non-creeping interbeds only transiently increase shear stress, whereas stiff, creep-active layers can preserve high differential stresses over abandonment time-scales, potentially governing the onset and location of failure.

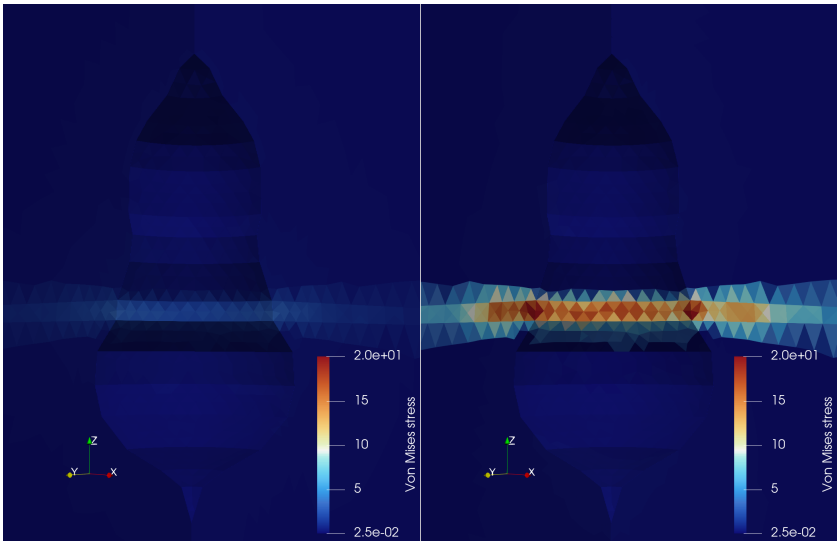

Figure B.4: Von Mises stress 300 years after abandonment for the interbed runs: claystone interbed (left) versus anhydrite interbed (right).